

## Measurement of muon-induced SEU cross sections and muonic X-rays for 65-nm SRAMs

馬原, 巧  
九州大学総合理工学府先端エネルギー理工学専攻

<https://hdl.handle.net/2324/4067225>

---

出版情報 : 九州大学, 2019, 修士, 修士  
バージョン :  
権利関係 :

2 0 1 9

## Master's Thesis

Department of Advanced Energy Engineering Science,  
Interdisciplinary Graduate School of Engineering Sciences,  
Kyushu University

Title

Measurement of muon-induced SEU cross sections  
and muonic X-rays for 65-nm SRAMs

Name

Takumi Mahara

Supervisor

Yukinobu Watanabe

# Contents

<b>1</b>	<b>Introduction</b>	<b>1</b>
1.1	Soft Error . . . . .	1
1.2	Mechanism of Single Event Upset in SRAM . . . . .	1
1.3	Cosmic-Rays and Soft Errors at Ground Level . . . . .	2
1.4	Characteristic of Muons . . . . .	4
1.4.1	Basic properties of muons . . . . .	4
1.4.2	Negative muon capture reaction . . . . .	5
1.4.3	Muonic X-ray . . . . .	7
1.5	Previous Works . . . . .	9
1.6	Objective . . . . .	12
<b>2</b>	<b>Experiment</b>	<b>14</b>
2.1	Muon Science Innovation Channel (MuSIC) . . . . .	14
2.2	Device under Test . . . . .	14
2.3	Experimental Setup . . . . .	15
2.4	Detectors and DAQ System . . . . .	16
2.4.1	Plastic scintillator . . . . .	16
2.4.2	Germanium detector . . . . .	18
2.4.3	Data acquisition system . . . . .	19
2.5	Experimental Procedure . . . . .	20
<b>3</b>	<b>Data Analysis</b>	<b>21</b>
3.1	SEU Cross Section . . . . .	21
3.1.1	Output signal from Plastic scintillator . . . . .	21
3.1.2	Dead time . . . . .	23
3.1.3	Statistical error of the number of upset bits . . . . .	23
3.1.4	Time synchronization between DAQ and VLSI tester . . . . .	23
3.2	Analysis of Muonic X-rays . . . . .	25
3.2.1	Standard source measurement . . . . .	26
3.2.2	Energy calibration . . . . .	28
3.2.3	Detection efficiency . . . . .	28
3.2.4	Identification of muonic X-rays generation positions . . . . .	30
<b>4</b>	<b>Experimental Results and Discussion</b>	<b>34</b>
4.1	SEU Cross Section . . . . .	34
4.1.1	Background run . . . . .	34
4.1.2	Momentum and operating voltage dependence . . . . .	34
4.2	Muonic X-ray . . . . .	39

<b>5</b>	<b>Simulation</b>	<b>41</b>
5.1	Method . . . . .	41
5.1.1	Sensitive volume model . . . . .	41
5.1.2	Simulation procedure . . . . .	41
5.2	Simulation Result . . . . .	43
5.2.1	SEU simulation . . . . .	43
5.2.2	Muonic X-ray simulation . . . . .	45
<b>6</b>	<b>Summary and Conclusion</b>	<b>46</b>

# Chapter 1

## Introduction

### 1.1 Soft Error

It is aimed that Society 5.0 will be achieved and implemented by 2030 as described in the 5th Science and Technology Basic Plan, which were approved in 2016, in Japan. While people have got the data and analyzed them by accessing the cloud in the information society (Society 4.0), in Society 5.0, Artificial Intelligence (AI) analyzes Big data from Internet of Things (IoT) devices. The analysis results are fed back to us through machines such as industry equipment, smart home applications, autonomous cars and so on. The number of IoT devices is expected to dramatically increase as shown in Figure 1.1 and the number is expected to exceed 400 billion by 2021. In particular, a rapid growth is expected in the categories whose errors affect human life, such as automobile, medical and industry as shown in Figure 1.2. It will be more important to evaluate and guarantee the reliability of the devices used in these categories.

Regarding the reliability of the devices, soft errors have recently been drawing attention. The radiation-induced soft errors mean a temporary faults in very large scale integrated (VLSI) circuit due to single event upset (SEU), i.e., upset of memory information in a static random access memory (SRAM) caused by the transient signal induced by radiation such as cosmic-rays. Originally, a soft error was regarded as a phenomenon which occurred only in outer space where high-energy cosmic-rays flow. However, from late 1990s, there has been decreasing tolerance of devices against soft errors in terrestrial environment since the miniaturization and integration of semiconductors have been advanced in accordance with Moore's law [2] and the radiation tolerance of semiconductors have been reduced accordingly.

### 1.2 Mechanism of Single Event Upset in SRAM

Figure 1.3 shows a physical and circuit process of a single event upset induced in an SRAM. 1-bit information is stored by the combination of the four MOSFET states. In this section, a situation as an example is described that the state of an SRAM with initial one of '1' is changed to '0'. When a charged particle passes through an nMOSFET with the initial state of "OFF", electron-hole pairs are generated along the incident particle path via Coulomb interaction between the particle and the electrons in orbit of atoms (mainly silicon). Then, the deposited charge caused by the interaction

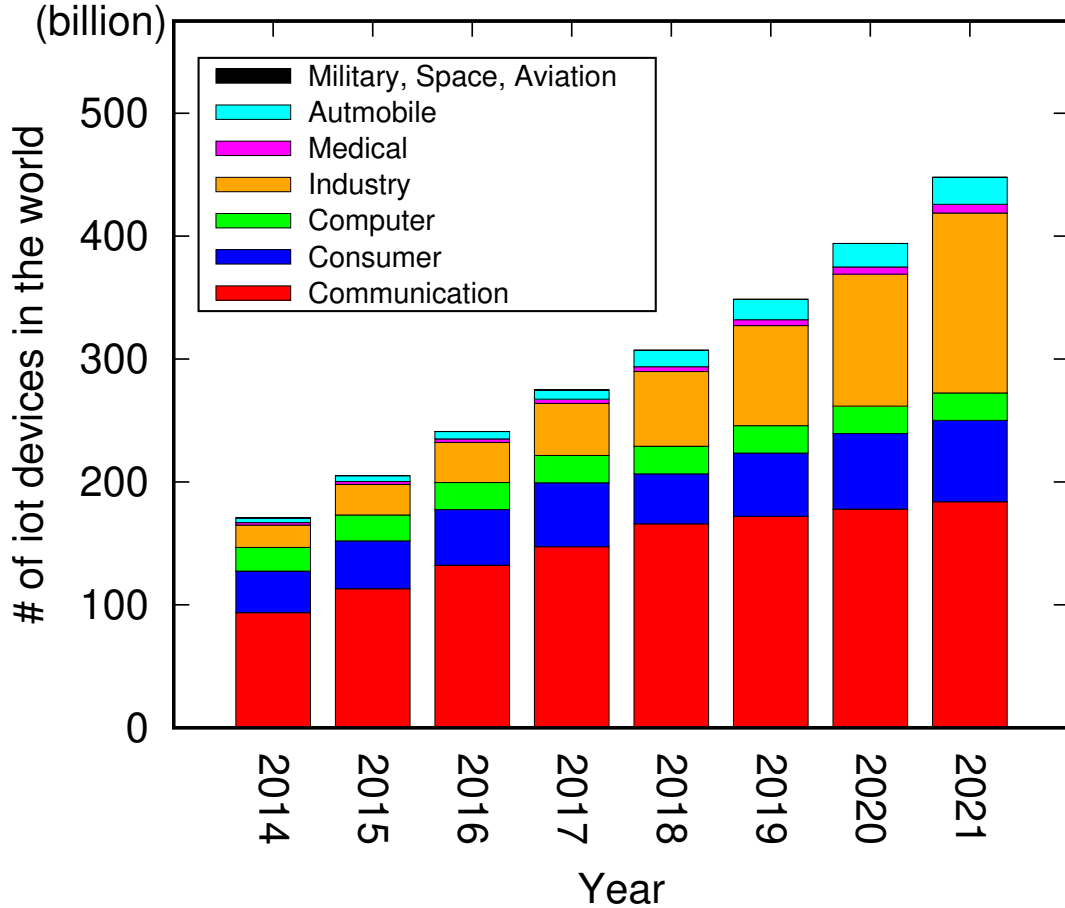


Figure 1.1: Trend of the number of IoT devices in the world [1].

is collected to drain region in Figure 1.3. When the collected charge exceeds the critical charge ( $Q_c$ ) which is defined as minimum charge to induce the SEU, the state of the nMOSFET which the particle enter is changed to “ON”. Then, the voltage of each MOSFET is changed and their states are immediately changed, and finally, the state of the SRAM is inverted to ‘0’.

### 1.3 Cosmic-Rays and Soft Errors at Ground Level

The secondary cosmic-rays have been recognized as a cause of soft errors in terrestrial environment. Figure 1.4 shows a schematic illustration of generation process of secondary cosmic-rays. The primary cosmic-rays (mainly protons) represent the high-energy particle generated via galaxy activities (supernova explosions, solar wind, etc.) in outer space. When the primary cosmic-rays enter the atmosphere of the earth, some of them induce nuclear reaction with nuclei (mainly nitrogen and oxygen) in the atmosphere, then secondary cosmic-rays are generated. Some of them finally reach the ground. Figure 1.5 shows their energy spectra at ground level calculated by Excel-based Program for calculating Atmospheric Cosmic-ray Spectrum (EXPACS) [3]–[5]. Among secondary cosmic-rays, muons are known to be major secondary cosmic-rays

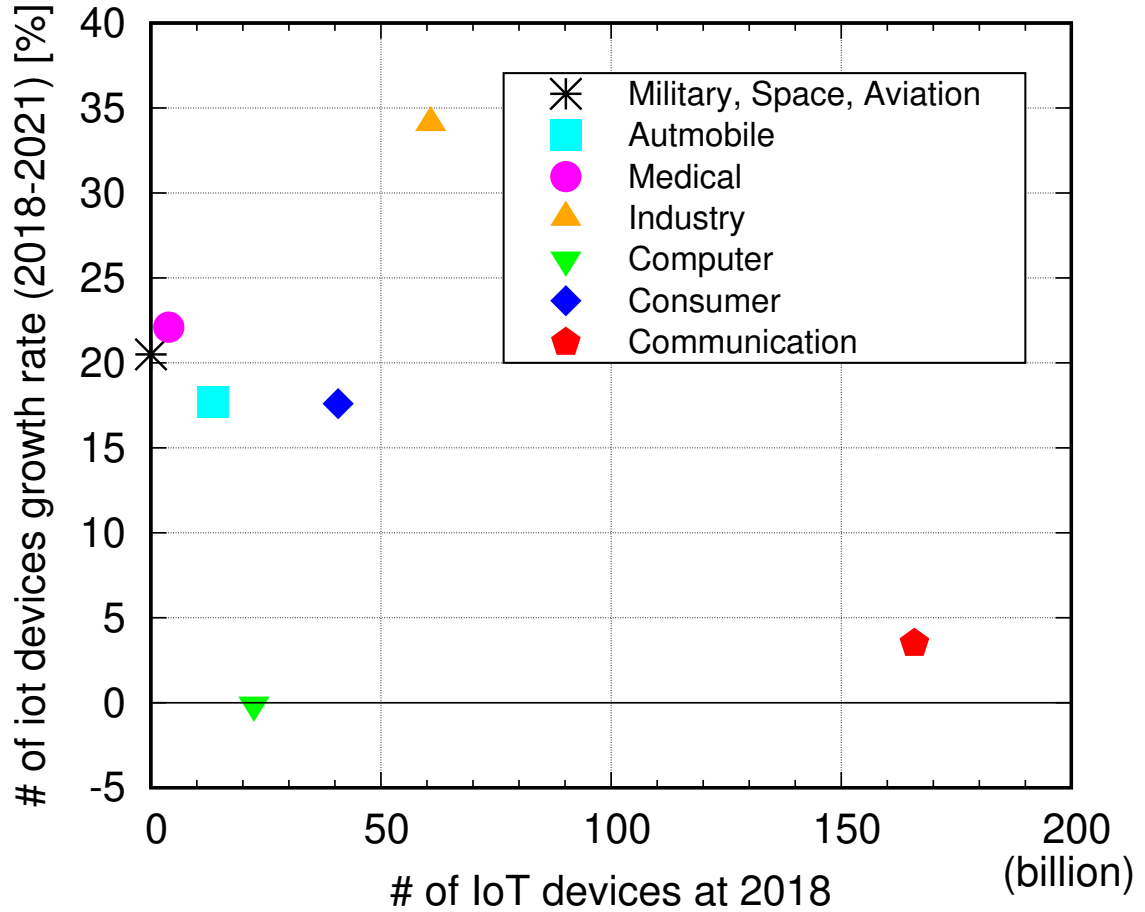


Figure 1.2: Growth rate of the number of IoT devices in the world [1]. The horizontal axis represents the number of IoT devices at 2018.

at ground level and their fraction is about three-quarter of the total cosmic-ray flux. The average muon kinetic energy is a few GeV as shown in Figure 1.5.

The cosmic-ray neutrons have been recognized as main factor particles of soft errors at ground level. Neutrons are uncharged particles so that they do not ionize matter and deposit charge directly. However, due to nuclear reactions with the atoms of materials, they can produce secondary ions and deposit sufficient charge to induce SEUs by indirect ionization.

On the other hand, muons have not been recognized as factor particles of soft errors since they rarely deposit charge which exceeds  $Q_c$  because of their high kinetic energy and small stopping power. However, recently, muon-induced soft errors are drawing attention due to decrease in  $Q_c$  and reduction of soft error immunity caused by the miniaturization and integration of semiconductors [6]–[18]. The studies of muon-induced soft errors are reviewed briefly in Section 1.5.

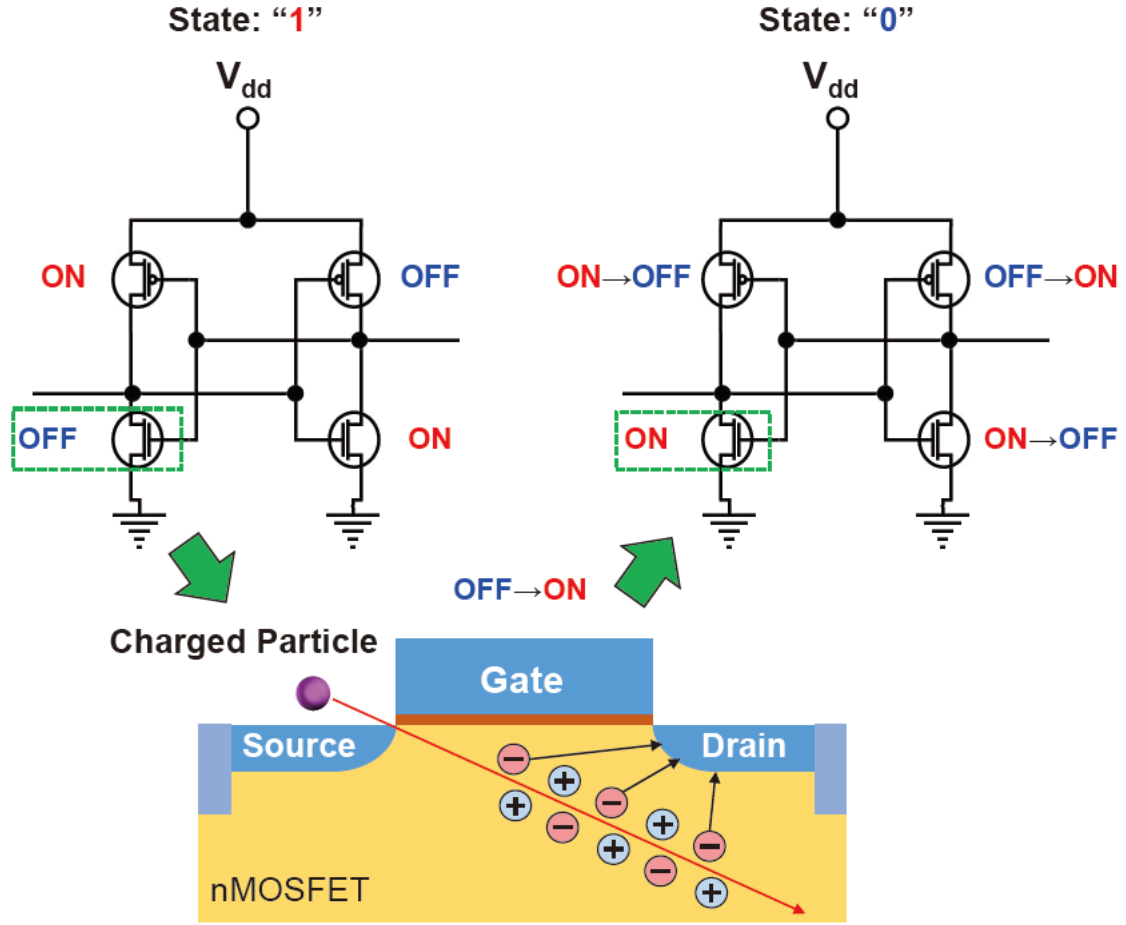


Figure 1.3: Schematic illustration of a single event upset induced by a charged particle. This figure shows the situation that a charged particle enter an nMOSFET.

## 1.4 Characteristic of Muons

Muons have positive or negative charge (named positive muon  $\mu^+$  and negative muon  $\mu^-$ , respectively) equal to the elementary charge. They are unstable element particles having mean lifetime of  $2.2 \mu\text{sec}$  and mass of  $105.7 \text{ MeV}/c^2$ . Therefore, muons are often called “heavy electrons” (electron mass is  $0.511 \text{ MeV}/c^2$ ). In this section, the physics of muons such as their production, decay process and interaction with matter are introduced.

### 1.4.1 Basic properties of muons

Muons are produced in the decay of pions ( $\pi^\pm$ ) or kaons ( $K^\pm$ ) according to:

$$\begin{aligned}
 \pi^+ &\rightarrow \mu^+ + \nu_\mu, \\
 \pi^- &\rightarrow \mu^- + \bar{\nu}_\mu, \\
 K^+ &\rightarrow \mu^+ + \nu_\mu, \\
 K^- &\rightarrow \mu^- + \bar{\nu}_\mu,
 \end{aligned} \tag{1.1}$$

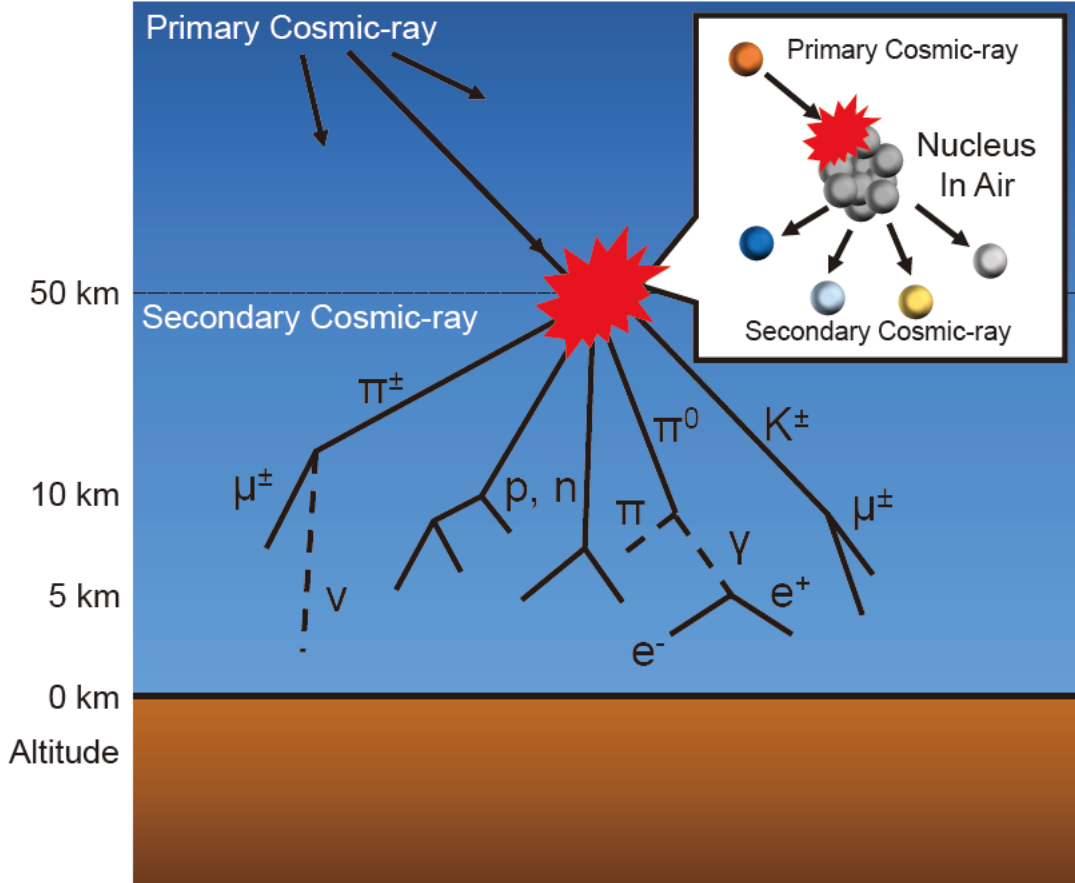


Figure 1.4: Generation process of secondary cosmic-rays.

where  $\nu_\mu$  and  $\bar{\nu}_\mu$  represent muon neutrino and anti-muon neutrino, respectively. Muons are unstable particles and decay with the mean lifetime of  $2.2 \mu\text{sec}$  according to:

$$\begin{aligned}\mu^+ &\rightarrow e^+ + \nu_e + \bar{\nu}_\mu, \\ \mu^- &\rightarrow e^- + \bar{\nu}_e + \nu_\mu,\end{aligned}\tag{1.2}$$

where  $\nu_e$  and  $\bar{\nu}_e$  represent electron neutrino and anti-electron neutrino, respectively.

### 1.4.2 Negative muon capture reaction

Both positive and negative muons pass through matter while losing their kinetic energy by generating electron-hole pairs along their track like other charged particles. While positive muons decay into positrons after losing incident kinetic energy and stopping according to Eq. (1.2), some negative muons are captured by an atom in matter via negative muon capture reaction [19]. The process of the reaction consists of two stages; atomic and nuclear muon capture. Figure 1.6 schematically shows the negative muon capture reaction process. When a negative muon stops in matter, it is captured by an atom in matter into high orbital momentum state and form a *muonic atom* according to the atomic muon capture. The captured muon cascades down to the 1s orbital while emitting Auger electrons or muonic X-rays since all low-lying orbital state are unoccupied. Since the time taken by a captured muon to cascades down to the 1s

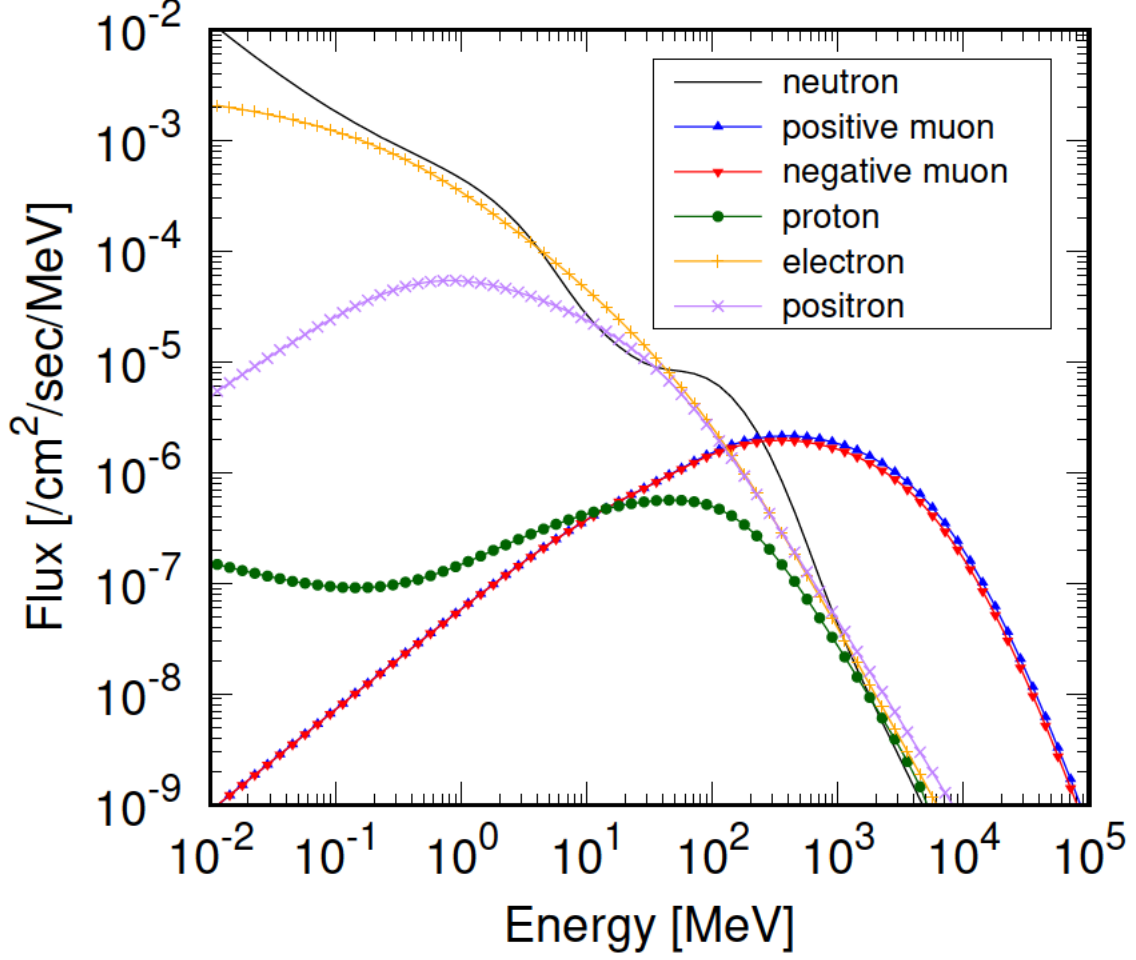


Figure 1.5: Energy spectra of secondary cosmic-rays at ground level calculated by EXPACS ver. 3.03. This figure shows the energy-spectra at Fukuoka, Japan.

orbital (about 100 fsec  $\sim$  1 nsec) [20] is negligible compared to its mean lifetime, almost all negative muons cascades down to the 1s orbital. While a part of captured negative muons decay into an electron and two neutrinos in the 1s orbital according to Eq. (1.2), the other muons react with protons in the nucleus according to:

$$\mu^- + p \rightarrow n + \nu_\mu, \quad (1.3)$$

where  $p$  and  $n$  represent proton and neutron, respectively. Then, a highly-excited nucleus is formed by the nuclear muon capture. In the case of  $^{28}\text{Si}$ , about 65% of negative muons stopped in matter are captured by a nucleus. Then, the excited aluminium nucleus are produced with excitation energy of 100.5 MeV in the following way:

$$\mu^- + {}^{28}\text{Si} \rightarrow {}^{28}\text{Al}^* + \nu_\mu + 100.5 \text{ MeV}. \quad (1.4)$$

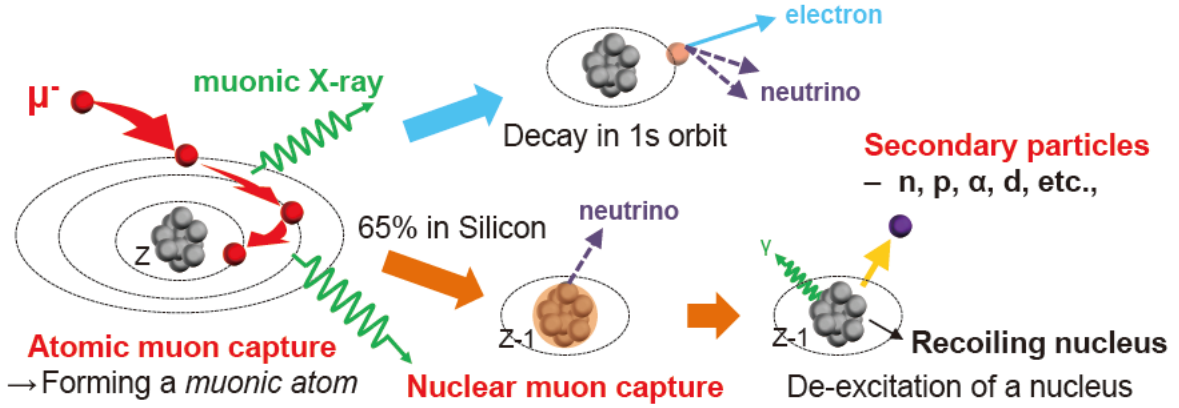
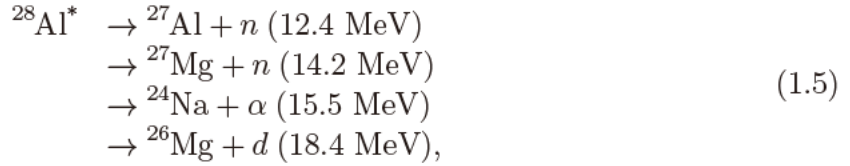


Figure 1.6: Schematic illustration of the negative muon capture process.

After that, secondary light particles (neutrons, protons,  $\alpha$  particles, deuterons, etc.) are emitted via de-excitation of  $^{28}\text{Al}^*$  as follows:



where  $\alpha$  and  $d$  represent  $\alpha$  particle and deuteron, respectively. The secondary ions emitted by the capture reaction have higher stopping power than muons themselves as shown in Figure 1.7.

### 1.4.3 Muonic X-ray

When a negative muon stopping in matter and captured by an atom cascades down to low orbital momentum, muonic X-rays or Auger electrons are emitted. Their energy corresponds to the difference between the orbital energy. The muonic X-ray and Auger electron emission compete in atomic muon capture. The probability of emitting muonic X-rays increases as the atomic number  $Z$  increases. Therefore, the muonic X-rays emission process is dominant for heavy atoms while the Auger electron one is dominant for light ones.

It is possible to roughly calculate the energy of muonic X-rays using the Bohr's model. Firstly, by assuming that the orbital negative muons have circular orbits, the quantum condition is described as follows:

$$\begin{aligned}
 \oint p dq &= p \cdot 2\pi a \\
 &= nh,
 \end{aligned} \tag{1.6}$$

where  $p$ ,  $q$  and  $a$  represent the momentum, coordinate variable and orbit radius of muons in the circular orbit, respectively,  $n$  represents the principal quantum number ( $n = 1, 2, 3, \dots$ ) and  $h$  represents the Planck constant ( $= 4.136 \times 10^{-21} \text{ MeV} \cdot \text{c}$ ). On

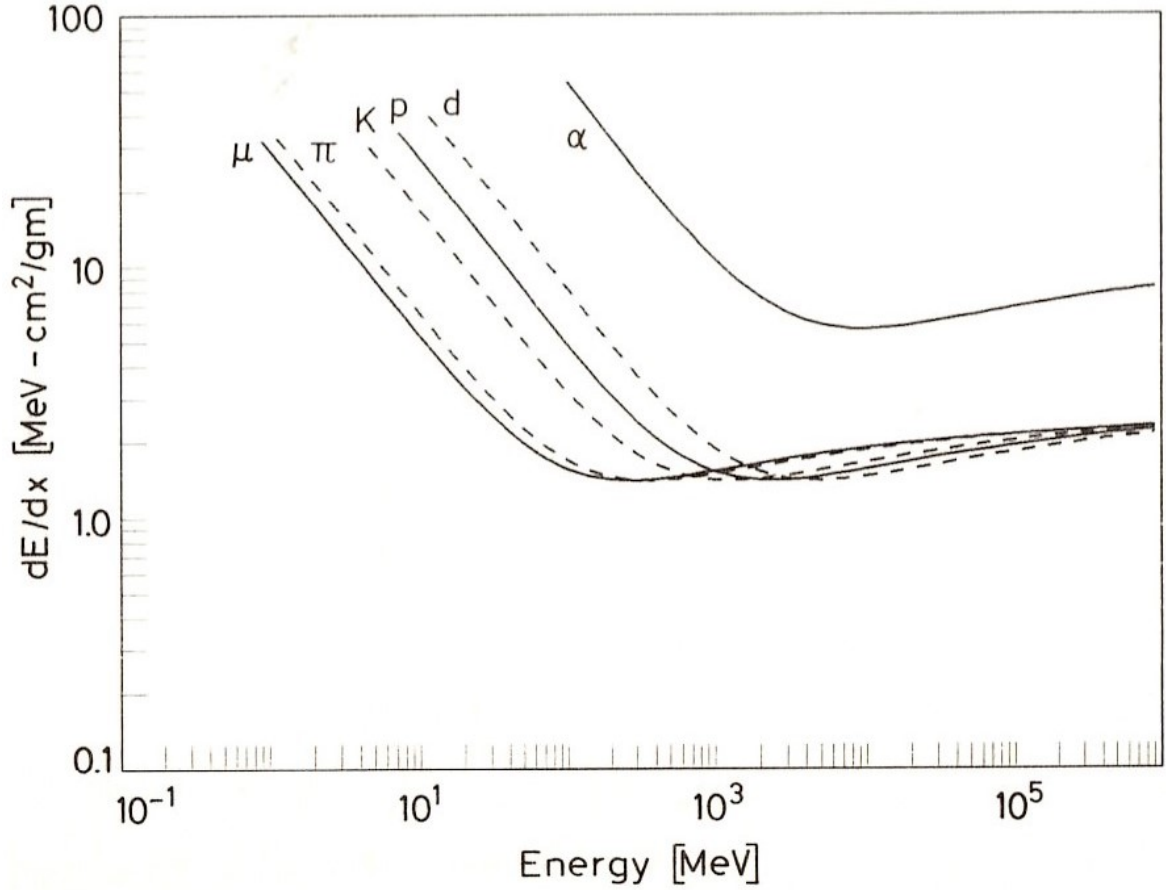


Figure 1.7: Stopping power  $dE/dx$  as function the energy of different particles. The figure is obtained from Fig. 2.4. in pp. 27 from [21].

the other hand, the following equation is derived from the balance between Coulomb and centrifugal forces:

$$\frac{p^2}{m_\mu a} = \frac{Ze^2}{4\pi\epsilon_0 a^2}, \quad (1.7)$$

where  $m_\mu$ ,  $e$  and  $\epsilon_0$  are the masses of muons ( $= 105.7 \text{ MeV}/c^2$ ), elementary charge ( $= 1.602 \times 10^{-19} \text{ C}$ ) and electric constant ( $= 8.854 \times 10^{-12} \text{ F/m}$ ). Then,  $a$  is derived by combing Eq. (1.6) and (1.7) as follows:

$$a = \frac{\epsilon_0 n^2 h^2}{\pi m_\mu Z e^2}. \quad (1.8)$$

The energy level in the principal quantum number of  $n$  ( $E_n$ ) is expressed as the sum of the kinetic and potential energy as follows:

$$\begin{aligned} E_n &= \frac{p^2}{2m_\mu} - \frac{Ze^2}{4\pi\epsilon_0 a} \\ &= -\frac{m_\mu Z^2 e^4}{8\epsilon_0^2 n^2 h^2}, \end{aligned} \quad (1.9)$$

Therefore, the energy of muonic X-rays emitted when muons transition from an orbit whose principal number of  $n_2$  to that of  $n_1$  with  $n_2 > n_1$  ( $E_{n_2 \rightarrow n_1}$ ) is given by:

$$\begin{aligned} E_{n_2 \rightarrow n_1} &= E_{n_2} - E_{n_1} \\ &= -\frac{m_\mu Z^2 e^4}{8\epsilon_0^2 n^2 h^2} \left( \frac{1}{n_1^2} - \frac{1}{n_2^2} \right), \end{aligned} \quad (1.10)$$

The energy of muonic X-rays is unique to the atomic number  $Z$  of the captured element as shown in Eq. (1.10). Therefore, the element existing in the stopping position of the negative muon can be identified by the measurement of the muonic X-ray energy in a non-destructive way. In addition, the stopping position is determined by initial muon momentum. Therefore, recently, in-depth elemental analysis of meteorites and archeological samples have been performed using negative muon beam [22], [23].

Muonic X-rays are named spectroscopically due to the transition process. For example, in the case of transition from  $n = 2, 3, 4$  to  $n = 1$ , the names are  $K\alpha$ ,  $K\beta$  and  $K\gamma$ . In addition, in the case of transition from  $n = 4$  to  $n = 2, 3$ , the names are  $L\beta$  and  $M\alpha$ . In this study, the notation of muonic X-rays mentioned above is used hereinafter.

## 1.5 Previous Works

Recently, a lot of works have been devoted to investigate the effect of cosmic-ray muons on the occurrence of SEUs. Table 1.1 shows a list of irradiation tests using low-energy muon. Positive muon irradiation tests were performed at the Tri-University Meson

Table 1.1: A list of muon irradiation tests from 2010

Authors	Facility	$\mu^+$ or $\mu^-$	Device	Ref.
Sierawski et al	TRIUMF	$\mu^+$	65, 55, 45-nm SRAM	[6], [7]
Sierawski et al	RIKEN-RAL	$\mu^+$	28-nm SRAM	[8]
N. Seifert et al	TRIUMF	$\mu^+$	32-nm planar & 22, 14-nm 3D Tri-Gate	[9]
G. Gasiot et al	TRIUMF	$\mu^+$	28-nm UTBB FDSOI & Bulk	[10]
J. M. Trippe et al	TRIUMF	$\mu^+$	28-nm SRAM	[11]
M. Bagatin et al	RIKEN-RAL	$\mu^+$	16-nm NAND Flash Memory	[12]
S. Manabe et al	MUSE	$\mu^{+/-}$	65-nm UTBB SOI SRAM	[14]
W. Liao et al	MUSE	$\mu^{+/-}$	65-nm Bulk SRAM	[15]
W. Liao et al	MUSE	$\mu^{+/-}$	65, 28-nm Bulk SRAM	[18]

Facility (TRIUMF) and RIKEN-Rutherford Appleton ISIS facility (RIKEN-RAL) [6]–[12] and the effect of direct ionization by positive muons on SEUs for some devices was investigated. In addition, a simulation work was performed to investigate the effect of low-energy negative muon on SEUs in 65-nm SRAMs[13]. The result of the simulation suggested that the recoiling nucleus and secondary ions emitted via negative muon capture reaction, which is mentioned in Section 1.4.2, cause SEUs significantly if muons are stopped and captured by nuclei near the sensitive drain region.

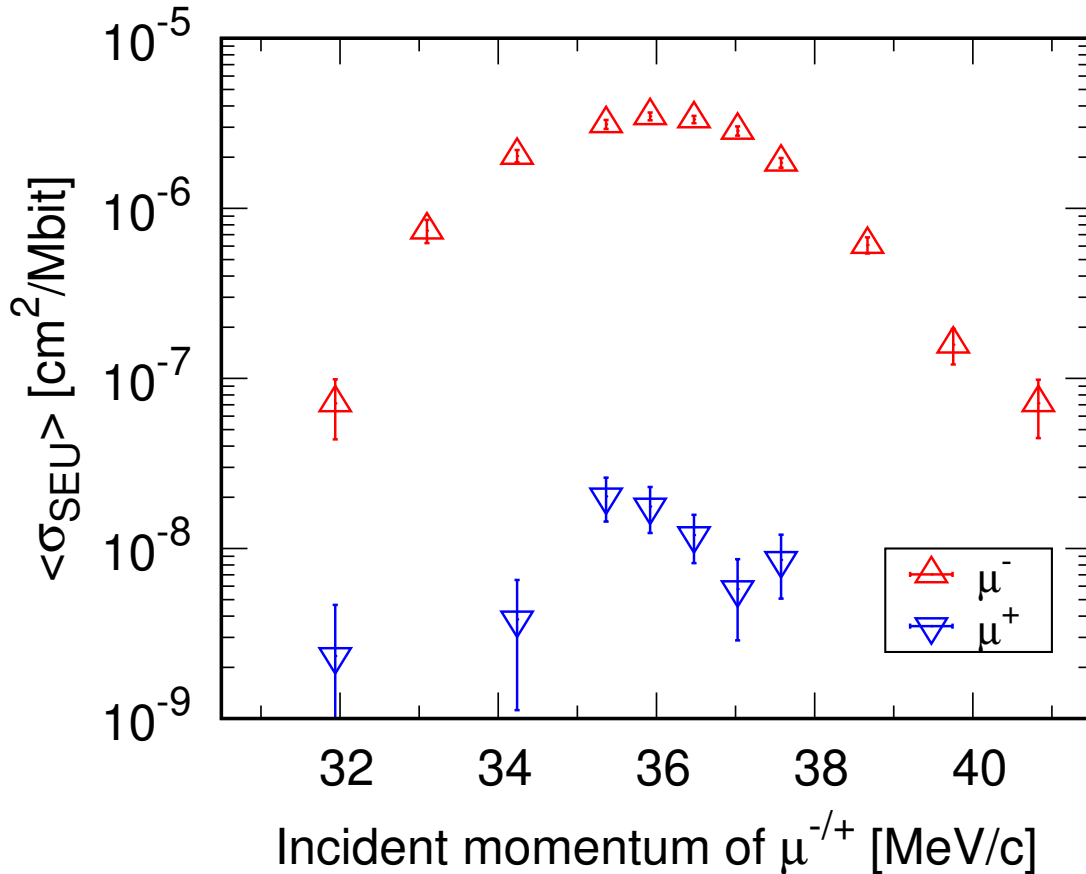


Figure 1.8: Incident momentum dependence of muon-induced SEU cross sections obtained at MUSE [15], [17]. The SRAM chips were operated at the voltage of 0.9 V. The negative muon-induced SEU cross sections are about 100 times larger than the positive muon-induced ones.

Our research group performed an irradiation test of low-energy positive and negative muons on 65-nm ultra-thin body and thin buried oxide silicon-on-insulator (UTBB SOI) and bulk SRAMs at the muon science facility (MUSE) [24], [25] in Materials and Life Science Experimental Facility (MLF) of the Japan Proton Accelerator Research Complex (J-PARC). The SEU cross sections were obtained as the ratio of the number of bit errors to incident muon fluence as a function of muon momentum as shown in Figure 1.8. It was found experimentally that negative muons cause SEUs more significantly compared to positive muons because of the effect of negative muon capture reaction. Furthermore, it was suggested that negative muons have a significant effect on the occurrence of SEUs when the muons stopped near sensitive volumes (SVs) and they emit secondary ions via the capture reaction using Particle and Heavy Ion Transport System (PHITS) [26] simulation. In addition, the operating voltage dependence for the SRAM chips was investigated in the previous work done at MUSE as shown in Figure 1.9. The result shows that there is a difference in the trend seen between positive muons and negative muons. The positive muon-induced SEU cross sections decrease as the operating voltage increases since the critical charge  $Q_c$  increases with an increase

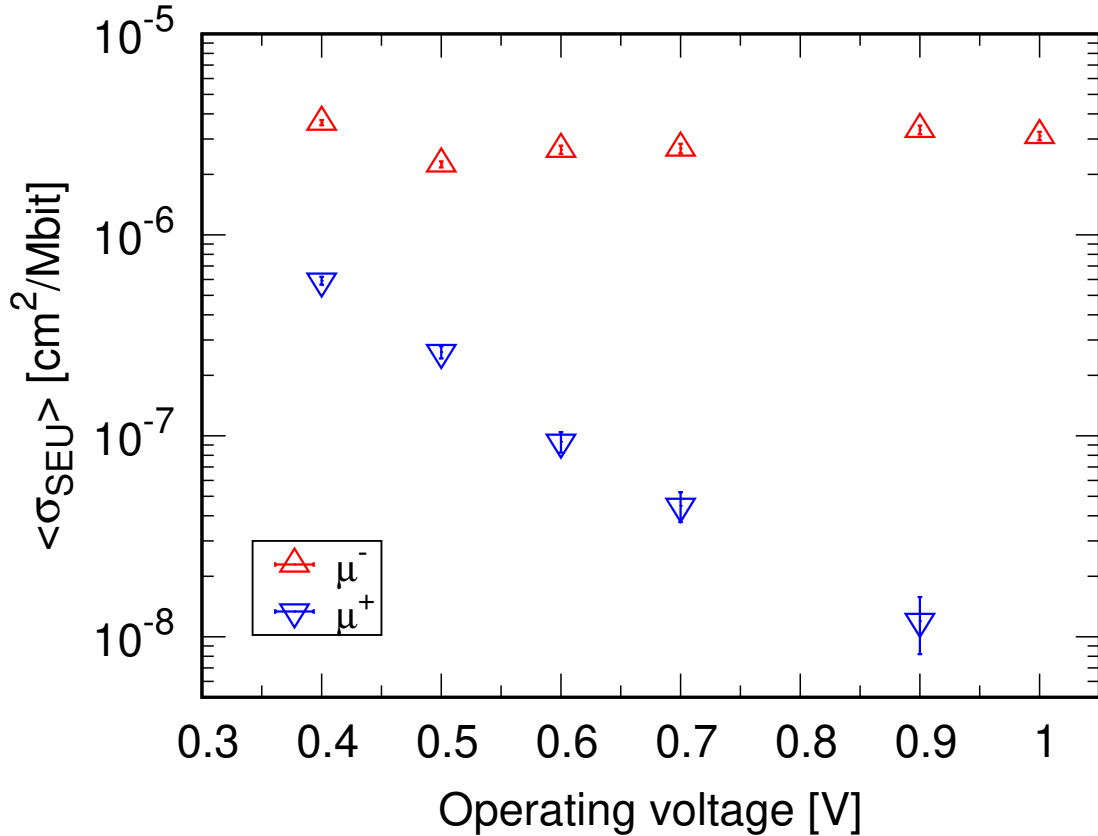


Figure 1.9: Operating voltage dependence of muon-induced SEU cross sections obtained at MUSE [15], [17]. The mean momentum of muons is 36.5 MeV/c.

of the operating voltage. On the other hand, the negative muon-induced SEU cross sections reach a minimum at 0.5 V and increase above 0.5 V. In [17], the similarity of this trend between neutron and negative muon SEUs was discussed.

Furthermore, the muon SEU rates at ground level for the 65-nm SRAMs [14], [15] were estimated based on the experimental SEU cross section data, and compared with the neutron SEU rates of the same SRAMs in [16]. The result showed that the muon SEU rates are 0.1 ~ 1% of the neutron SEU rates. However, the relative proportion of the muon SEU rate to the neutron SEU rate was found to increase up to about 10% on the first floor of a five story building because of relatively large attenuation of neutron flux and less attenuation of muon flux in the building. In addition, a muon irradiation test [18] for 28-nm SRAMs revealed that the muon SEU cross section increases and the neutron SEU cross section decreases according to the technology advancement [27]. These recent works on muon induced SEUs require further study to enhance the understanding of the SEU mechanism.

There are two types of muon beam as shown in Figure 1.10. There are five muon irradiation facilities in the world and a pulse muon beam is available at J-PARC/MUSE in Japan and RIKEN-RAL in UK while a direct current (DC) muon beam is available at RCNP-MuSIC in Japan, TRIUMF in Canada and Paul Scherrer Institute (PSI) in Switzerland. The pulsed muon beam with a repetition rate of 25 Hz is available at MUSE. Approximately  $10^4$  muons were bunched in a pulse with about 100 nsec width

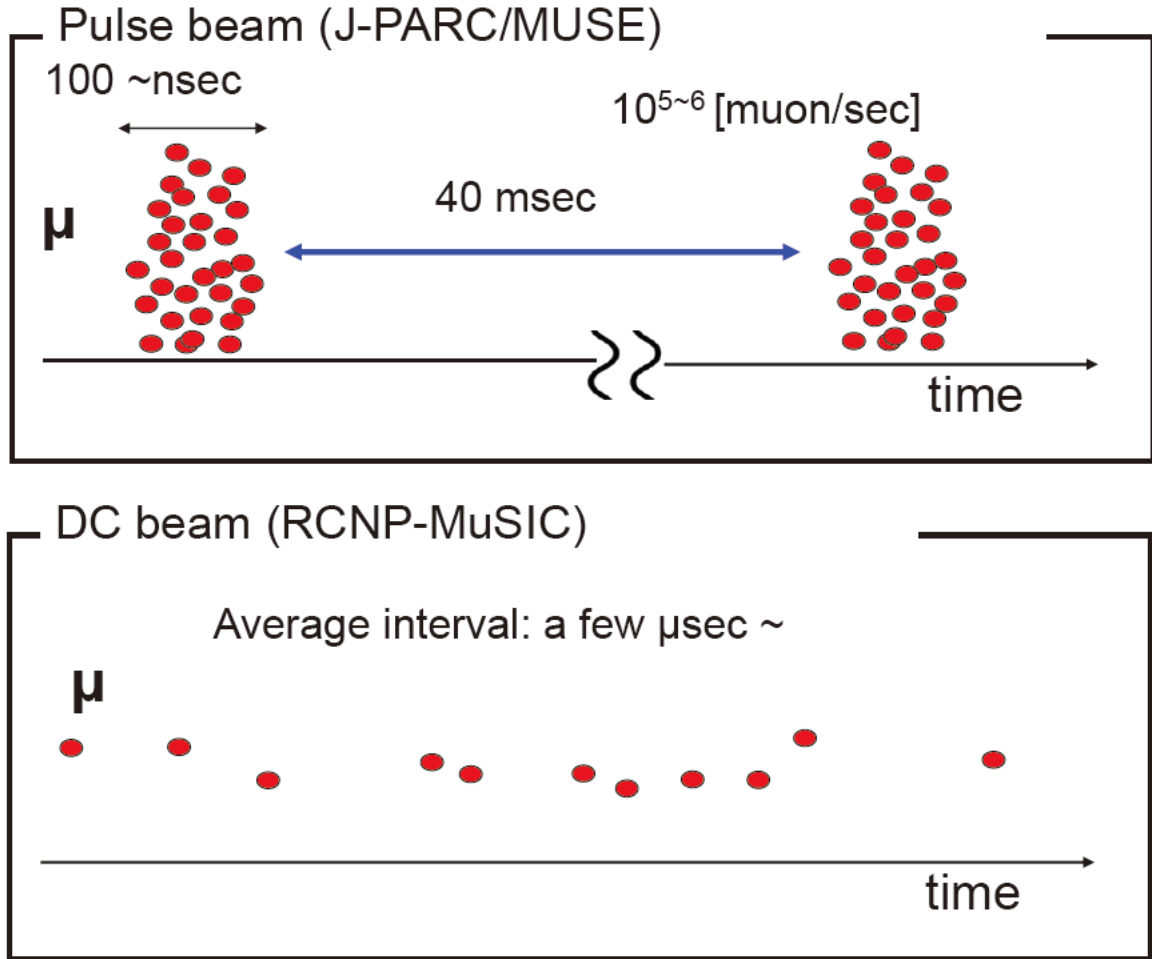


Figure 1.10: Schematic illustration of two types of muon beam.

during the previous experiment at MUSE [24], [25]. In this type of muon beam, high intensity muons are available. However, the pulse beam is not suitable to measure muon fluence directly since there are too many signals by muons in such a short time ( $\sim 100$  nsec in the case of MUSE) to acquire the data from them. Therefore, the muon fluence was indirectly measured by counting the number of decay electrons/positrons that were emitted from stopped muons according to Eq. (1.2) in the previous work at MUSE [14], [15]. Hence, there might be an uncertainty in the indirect measurement of muon fluence.

## 1.6 Objective

In this study, we performed a new experiment with a direct current (DC) muon beam at Muon Science Innovation Channel (MuSIC) [28] of Research Center for Nuclear Physics (RCNP), Osaka University to make the measured SEU cross sections more reliable. The MuSIC beam line provides the muon beam with a continuous time structure with the intensity of approximately  $2 \times 10^3$  muons/sec. Therefore, a single muon can be detected

individually and reliable absolute value of SEU cross sections can be obtained. The obtained SEU cross sections were compared with the those obtained in the previous work at MUSE from the view points of the dependence of momentum and operation voltage.

In addition to the SEU cross section measurement, muonic X-rays emitted from the device board were measured since DC muon beam is suitable for measurement of short-time ( $\sim 100$  nsec) physical phenomena such as muonic-X-rays. The previous work at MUSE pointed out that negative muons stopped near SVs has a significant effect on SEU. Therefore, information on the muon stopping position and constituent elements at its position is important to study the mechanisms of SEUs induced by negative muons. Thus, a measurement of muonic X-rays was performed to see the feasibility of elemental identification at the muon stopping position.

# Chapter 2

## Experiment

Negative and positive muon irradiation tests for the SRAMs were performed at Muon Science Innovation Channel (MuSIC)-M1 beam line of Research Center for Nuclear Physics (RCNP), Osaka University. In this chapter, the facility, devices, and detectors used in the experiment are described.

### 2.1 Muon Science Innovation Channel (MuSIC)

Figure 2.1 shows the bird's eye view of RCNP. A proton obtained from an ion source is accelerated to 392-MeV via two variable energy cyclotrons (AVF and Ring Cyclotron in Figure 2.1). The 392-MeV proton cyclotron was operated with the average current of  $1.1 \mu\text{A}$  during the experiment. Figure 2.2 shows the schematic illustration of MuSIC-M1 beam line. The proton beam is irradiated to a cylindrical graphite target (4 cm in diameter and 20 cm long) inside the solenoid coil in Pion Capture System and pions are generated through the nuclear reaction between them. The generated pions are collected by the 3.5-T capture solenoid magnet and transported by  $36^\circ$  curved solenoid into MuSIC-M1 Beam Line. During the transport, the pions decay into muons according to Eq. (1.1). Finally, the produced muons are transported to the downstream of MuSIC-M1 Beam Line.

The polarity and momentum of muons are selectable by a solenoid magnet by adjusting the polarity and current value of the capture solenoid. The momentum distribution of the muon beam at the beam exit was measured as a normal distribution with 7.0% standard deviation by using a time of flight method before the experiment [31].

### 2.2 Device under Test

The test SRAM chips were fabricated in 65-nm planar bulk complementary metal oxide semiconductor (CMOS) technology with a deep well option. Figure 2.3 shows the device board under test. The 16 SRAM chips are mounted on a piece of printed circuit board (PCB). Each chip has 12-Mbit memories. The same test board was used in the previous muon experiment at the MUSE facility [15].

As mentioned in Section 1.5, 65-nm UTBB SOI SRAMs were also used in the previous experiment. The UTBB SOI SRAM has higher SEU tolerance compared to

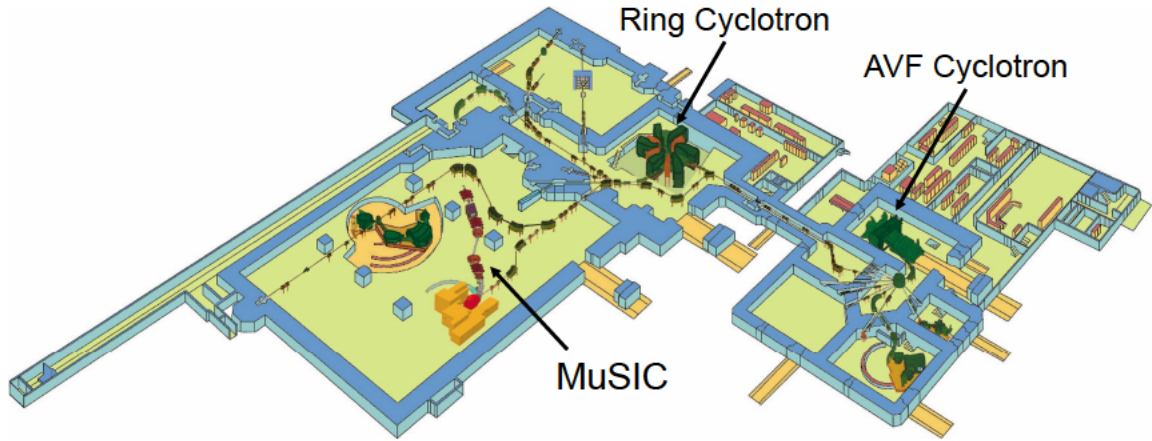


Figure 2.1: Bird's eye view of RCNP from [29]

the bulk one as reported in [16]. In addition, the intensity of muon beam at MuSIC is lower than that of MUSE. Therefore, UTBB SOI SRAMs were not used in the experiment because it takes long time to take the data with sufficient statistics.

## 2.3 Experimental Setup

Figure 2.4 shows a photograph of the experimental setup at M1 Beam Line. In the experiment, two kinds of detectors, plastic scintillators (PS) and Germanium (Ge) detectors, were used. One PS (forward PS) was placed at the upstream of the device board and the other PS (backward PS) and two Ge detectors (GLP36300 and BE2020 manufactured by ORTEC and CANBERRA, respectively) were placed at the downstream. The detail of the detectors used in the experiment is described in Section 2.4. Also, the VLSI tester was placed in the experimental area and connected to the device board to read/write the stored data in the SRAMs on the chips of the device board.

The configuration of muon irradiation and arrangement of detectors is schematically illustrated in Figure 2.5. The beam collimator was placed between the beam exit and the device board. The beam exit was equipped with a  $75\text{-}\mu\text{m}$ -thick Kapton film to seal a vacuum of the beam line. Figure 2.6 shows the structure of the beam collimator. The front aluminium plate was fixed vertically on the base plate. Piled lead blocks were placed on the base plate. The slit size of lead blocks and the front aluminium plate was  $55\text{ mm} \times 55\text{ mm}$ . All inner surfaces of the slit of lead blocks were covered with other  $10\text{-mm}$ -thick-aluminium plate. In addition,  $5\text{-mm}$ -thick aluminium plates are enough thick to stop incident muons fully in the experiment, i.e., all muons do not stop in the lead plates. Since the atomic number  $Z$  of Al is smaller than that of Pb, Al has lower nuclear capture rate of negative muons than Pb. Hence, the aluminium plates were chosen so that the emission of background particles (e.g., neutrons and light ions) via negative muon nuclear capture reaction in the plate can be reduced. The lead blocks play a role in the shielding of decay electrons/positrons from the aluminium plates and background  $\gamma$ -rays.

The all 16 chips, i.e., 192 Mbits SRAMs in the device board were irradiated in the experiment. For comparison with the previous study [15], the reverse side of the device

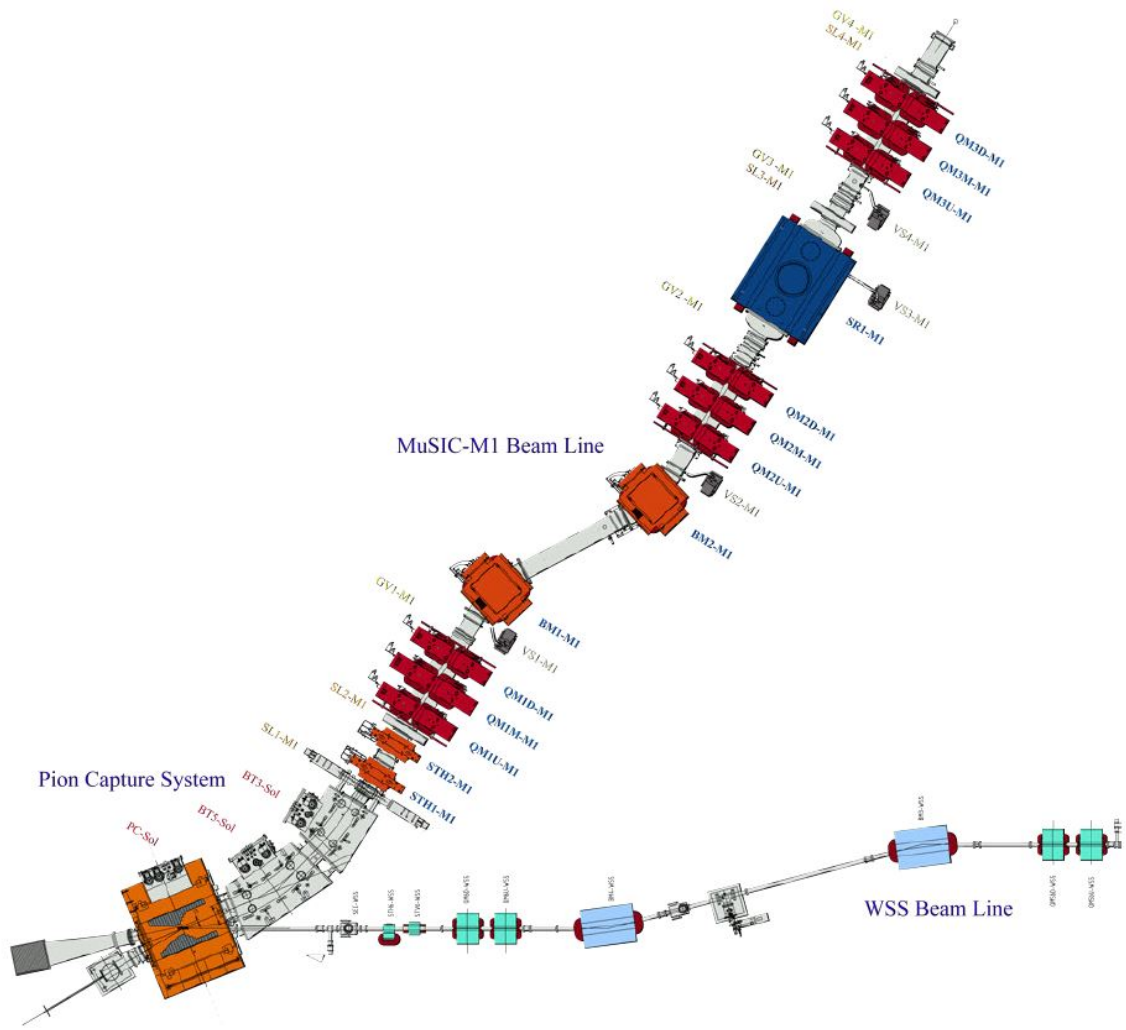


Figure 2.2: Schematic view of MuSIC-M1 beam line. WSS Beam Line mentions a beam line of protons. The figure is obtained from Figure 1 in [30]

board was irradiated with the muon passing through the collimator as shown in Figure 2.3.

## 2.4 Detectors and DAQ System

As shown in Figure 2.5, the detectors were placed at the downstream from the beam exit and signals from them were acquired and stored after the signal processing by the data acquisition (DAQ) system. In this section, the details of the detectors and DAQ system used in the experiment are described.

### 2.4.1 Plastic scintillator

Plastic scintillators (PSs) are the most widely-used organic scintillators because of their rapid response (a few nsec) and high detection efficiency. When a radiation passes

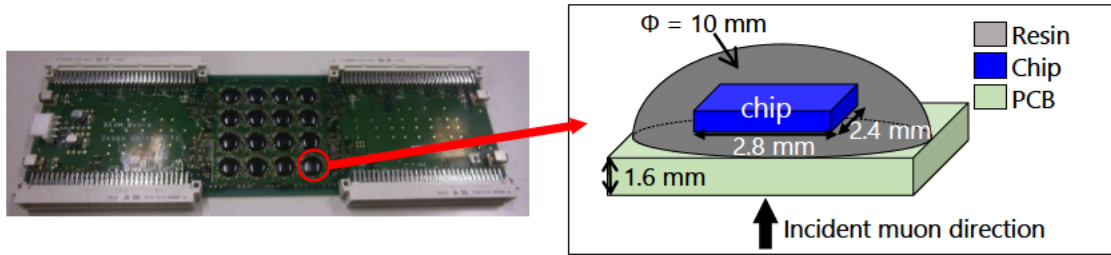


Figure 2.3: Structure of the test device board. 16 chips on the 1.6-mm-thick PCB. The thickness of tested chips approximately 0.34 mm.

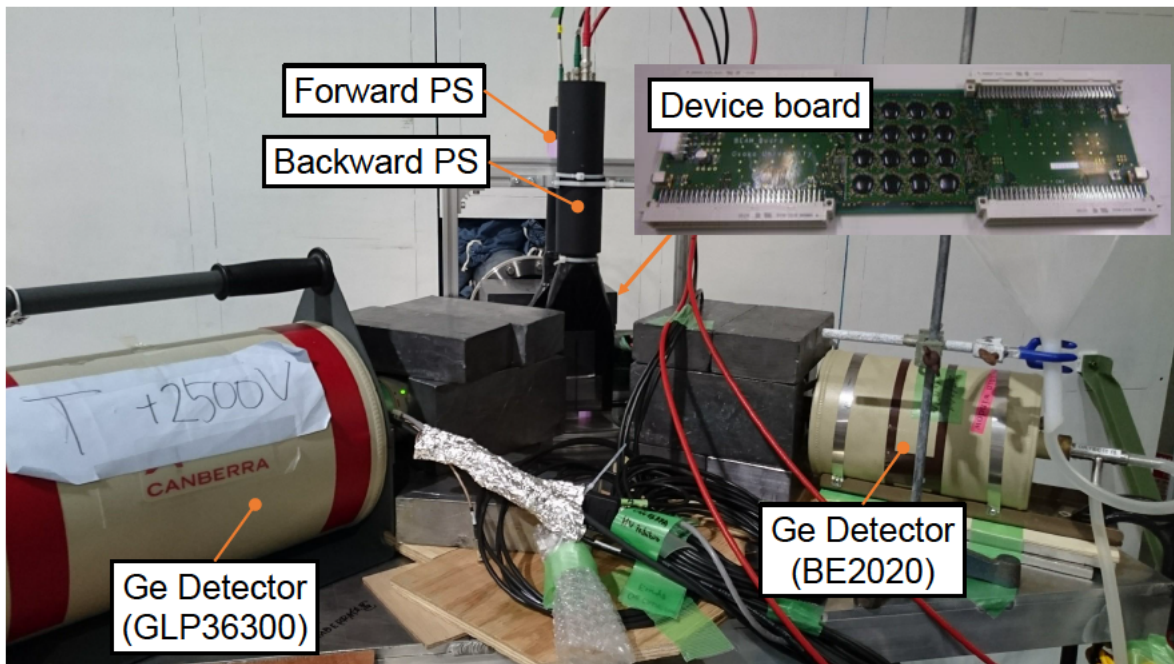


Figure 2.4: A photograph of the experimental setup from downstream.

through a PS, it excites the atoms and molecules in the PS, causing scintillation light output to be emitted. The light is transmitted to a photomultiplier tube (PMT) and converted to the current of photoelectrons. This current obtained in the experiment was amplified by the 572A Amplifier (Amp.) manufactured by ORTEC.

In the experiment, the size of the forward PS was 100 mm × 100 mm and the thickness was 0.4 mm. It was placed 1.3 mm from the device board at the upstream as shown in Figure 2.5. The incident muon fluence can be measured directly thanks to the DC muon beam by using the forward PS. In addition, the signals from the forward PS was used as the trigger to store the signals from the other detectors. On the other hand, the size of the backward PS was 100 mm × 100 mm and the thickness was 5 mm. The backward PS was placed from 145 mm at the downstream to detect muons which pass through the device board.

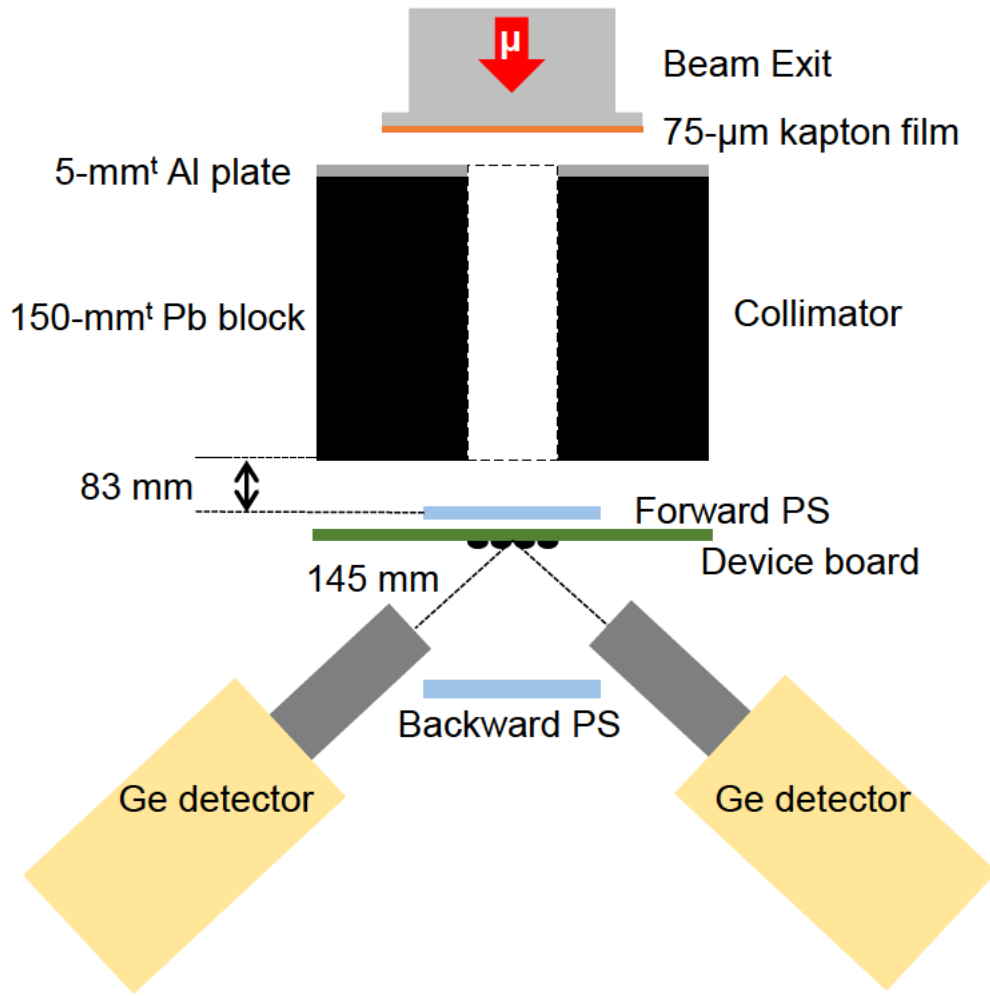


Figure 2.5: Configuration of muon irradiation and arrangement of detectors.

### 2.4.2 Germanium detector

Germanium detector (Ge detector) is a kind of semiconductor detector and mostly used for photons such as X-ray and  $\gamma$ -ray spectroscopy. Generally, the dose of detected photons in a semiconductor detector is counted by integrating the energy spectra around a peak caused by photoelectric effect between the photon and the semiconductor crystal in the detector. The photoelectric cross section increases as the atomic number  $Z$  of the crystal increases. Therefore, for photon detection, germanium is preferred over silicon because of its much higher  $Z$  ( $Z_{\text{Si}}=14$  and  $Z_{\text{Ge}}=32$ ). However, Ge detectors must be operated at low temperature because of their smaller band gap.

When photons interact with the material within the depleted volume of a detector, charge carriers (holes and electrons) are produced and are swept by the electric field to the P and N electrodes. This charge, which is in proportion to the energy deposited in the detector by the incoming photon, is saved as electric voltage by an integral charge sensitive preamplifier. The saved voltage must be re-convert in the energy after measurement, which is described in Section 3.2.2.

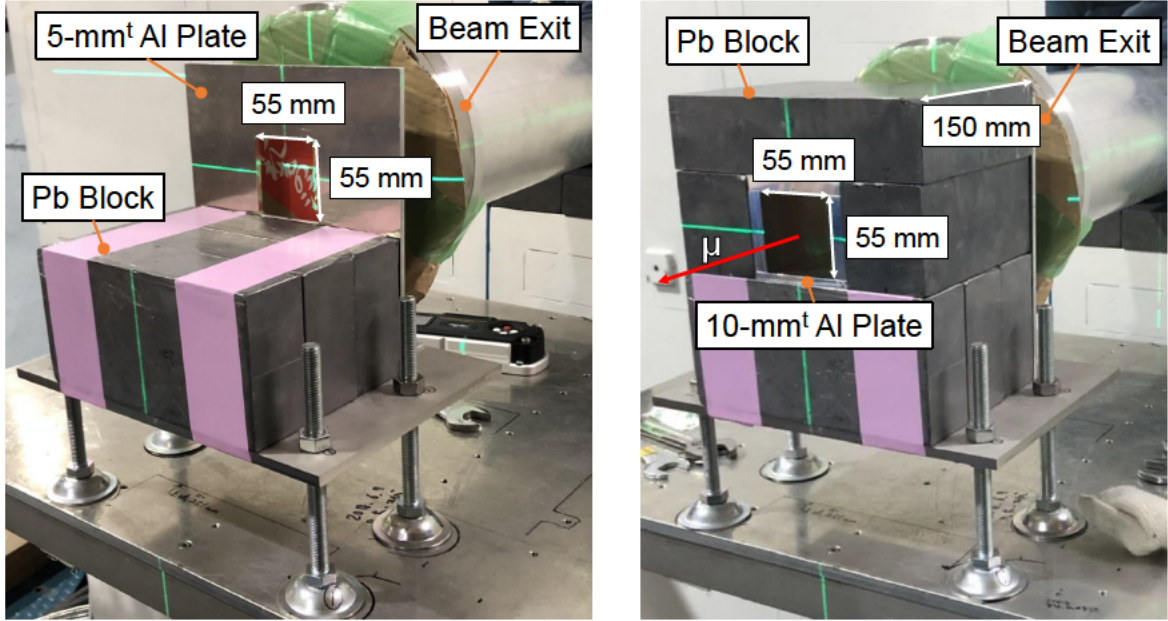


Figure 2.6: Photographs of the beam collimator.

In the experiment, the energy spectra of muonic X-rays were measured during muon irradiation on the device board. The dynamic range of both the Ge detectors was set to be about 1 MeV, which is large enough to detect 400-keV  $K\alpha$  muonic X-ray from silicon in the SRAM chips. In this dissertation, the data analysis and its result of muonic X-ray measurement by GLP36300, whose detection efficiency is larger than BE2020, is described.

### 2.4.3 Data acquisition system

In the experiment, the signals from PSs and Ge detectors are processed in the data acquisition (DAQ) system with NIM and VME modules. The signals from all detectors were sent to shaping amplifiers to obtain the energy information. The outputs from the amplifiers were fed into an Analog to Digital Converter (ADC, A3400 VME module manufactured by NIKIGLASS Co., LTD.) module and the pulse height of signals were recorded. The signal from the forward PS was sent to the discriminator (N-TM104 manufactured by Technoland Corp.) to generate a logic signal. The logic signal sent to DAQ master (VLUPO, see the cite [32]) as a trigger of the DAQ system. The DAQ master controlled A3400 VME module during the experiment. When a trigger signal was sent and A3400 VME module did not process any data, the trigger was accepted and A3400 VME module recorded the pulse height of all inputs.

The numbers of all trigger events and the events accepted by the DAQ master module were counted as the number of gated and un-gated triggers, respectively. They were recorded by the scaler module to evaluate the dead time as described in Section 3.1.2.

## 2.5 Experimental Procedure

The VLSI tester was used to obtain the number of bit errors during irradiation. The operation of the VLSI tester consists of three operations; “write”, “hold”, “read” operation. Firstly, the test SRAM memories are initialized by writing the data ‘0’ in the “write” operation with operating voltage of 1.2 V. Next, after reducing the voltage to test voltage (0.9, 0.5 and 0.4-V in the experiment), the operation moves to the “hold” operation for ten minutes. Finally, after increasing the voltage to 1.2 V, the data stored in the SRAM is read through and the number of bit errors is counted. In the experiment, the mean momentum of negative muon beam was changed from 37.8 MeV/c to 41.0 MeV/c (6.6 MeV to 7.7 MeV in the kinetic energy) at the beam exit. The momentum scanning run was carried out at the 0.9-V operating voltage of the SRAMs. In addition, the negative and positive muon-induced SEU cross sections were measured at the operating voltage of 0.5 and 0.4 V.

On the other hands, the forward PS and Ge detectors were used to count the number of the incident muons and muonic X-rays emitted from the irradiated device, respectively. When a signal from the forward PS was sent to the DAQ master module in the shape of a logic signal, the signals from detectors are begun to stored.

The DAQ system and VLSI tester were operated independently, so that the time synchronization is necessary between them and the detail is described in Section 3.1.4.

# Chapter 3

## Data Analysis

In this chapter, the data analysis of the present experiment is described.

### 3.1 SEU Cross Section

Muon-induced SEU cross sections of the SRAMs were derived by dividing the number of the observed upset bits  $N_{\text{SEU}}$  by the product of the incident muon fluence  $\Phi_{\text{muon}}$  and the total number of irradiated bits  $N_{\text{total}}$  (=192 Mbits) as expressed in the following formula:

$$\sigma_{\text{SEU}} = \frac{N_{\text{SEU}}}{\Phi_{\text{muon}} \cdot N_{\text{total}}}. \quad (3.1)$$

$N_{\text{SEU}}$  was simply acquired by the counting number of upset bits through the VLSI tester as mentioned in 2.5. Hence, a data analysis method of deriving  $\Phi_{\text{muon}}$  is described below. In addition, an evaluation method for the statistical error of  $N_{\text{SEU}}$  is also described in 3.1.3.

#### 3.1.1 Output signal from Plastic scintillator

The forward PS was used to measure the incident muon fluence. A pulse height of the analog output signal from the scintillator was converted to a digital value by the analog-to digital converter (ADC) as mentioned in Section 2.4.3. The ADC spectrum of the scintillator output is shown in Figure 3.1. The incident beam includes contaminated electrons which have the same momenta as the muons. The muon deposition energy in the PS is larger than the electron one. Hence, the peak of the muon events was observed in the higher channel range compared to those of the electron events as shown in Figure 3.1. To distinguish the muon events from all the other events, the threshold channel value was set to around 700 channels where the spectrum has the minimum value between the peaks of muons and electrons, and the events over the threshold were integrated to derive the incident muon fluence. To estimate the systematic uncertainty in the derivation of the incident muon fluence, two threshold channels were tentatively set to be 600 ch and 800 ch. However, the variation of the derived fluence was only 2%. As a result, the systematic error caused by the contamination of electrons in the incident muon fluences was assumed to be 2% in the present analysis.

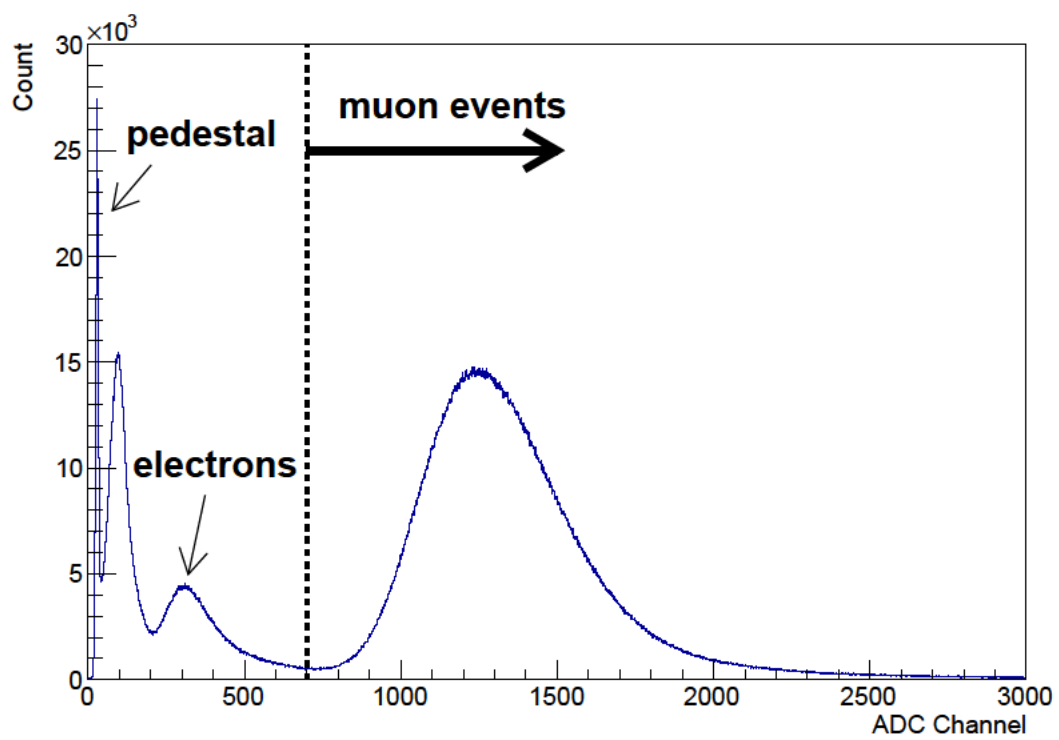


Figure 3.1: ADC spectrum of the forward plastic scintillator at the incident momentum of 38.9 MeV/c at beam exit.

### 3.1.2 Dead time

In radiation measurements, a detector signal generated by an incident particle is lost in the time period when the pulse generated by the previous incident one is detected and its signal is processed by data acquisition (DAQ) system. This time period during which the data is not recorded is called the dead time. The dead time is defined as the time periods during which a detector becomes insensitive to the next pulse by detection for the previous pulse and DAQ does not accept the next pulse because of processing a signal generated by the previous pulse. The response time of plastic scintillator is typically short as mentioned in Section 2.4.1, therefore, the dead time was caused mainly by the time for processing a signal in the DAQ in the experiment. Then,  $\Phi_{\text{muon}}$  was derived in consideration of the dead time correction using the following formula:

$$\Phi_{\text{muon}} = \frac{F_{\text{PS}}}{S} \times \frac{T_{\text{un-gated}}}{T_{\text{gated}}}, \quad (3.2)$$

where  $F_{\text{PS}}$  represents the number of detected events by integrating over 700 ch in the ADC spectrum of the scintillator output as shown in Figure 3.1,  $S$  is the area of irradiated part of device board ( $=5.5 \text{ cm} \times 5.5 \text{ cm}$ ) and  $T_{\text{un-gated}}$  and  $T_{\text{gated}}$  are the number of un-gated and gated triggers as mentioned in 2.5, respectively.

### 3.1.3 Statistical error of the number of upset bits

SEUs in SRAM are classified into Single Bit Upset (SBU) and Multiple Cells Upset (MCU). SBU refers to as a single SRAM bit upset at the injection of a single particle. On the other hand, multiple bits sometimes upsets at the injection of a single particle which have high stopping powers. This phenomenon is called MCU. The numbers of upset bits per a single event were recorded in the VLSI tester used in the experiment. Therefore,  $N_{\text{SEU}}$  can also be expressed by :

$$N_{\text{SEU}} = \sum_{i=1}^{\infty} i \times N_i, \quad (3.3)$$

where  $i$  represents the number of upset bits per a single event and  $N_i$  represents the number of events of  $i$ . Therefore, the statistical error of  $N_{\text{SEU}}$  can be evaluated as follows:

$$\begin{aligned} \Delta N_{\text{SEU}} &= \sqrt{(1 \times \sqrt{N_1})^2 + (2 \times \sqrt{N_2})^2 + \dots} \\ &= \sqrt{\sum_{i=1}^{\infty} i^2 \times N_i}, \end{aligned} \quad (3.4)$$

### 3.1.4 Time synchronization between DAQ and VLSI tester

In the experiment, the DAQ system was used to obtain the detected counts of incident muons and muonic X-rays while the VLSI tester was used to obtain the number of errors. The DAQ system and VLSI tester were operated independently. Therefore, it is necessary to synchronize both the data obtained by the DAQ and VLSI tester. An example of operating time for the DAQ and VLSI tester is depicted schematically in Figure 3.2. Normally, the DAQ system was almost always working while the VLSI

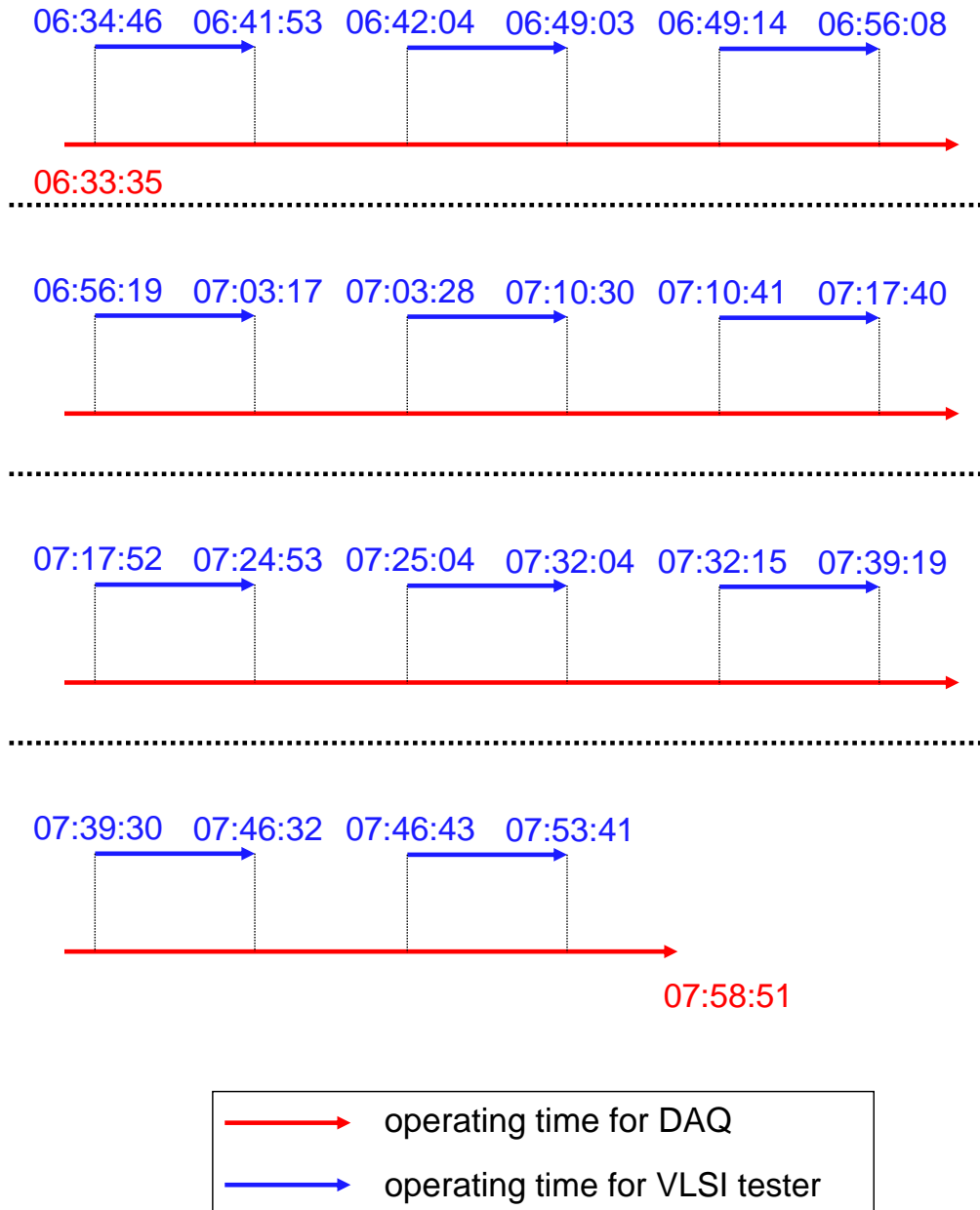


Figure 3.2: An example of schematic view of operating time for DAQ and VLSI tester. This run was performed at 6th June 2018.

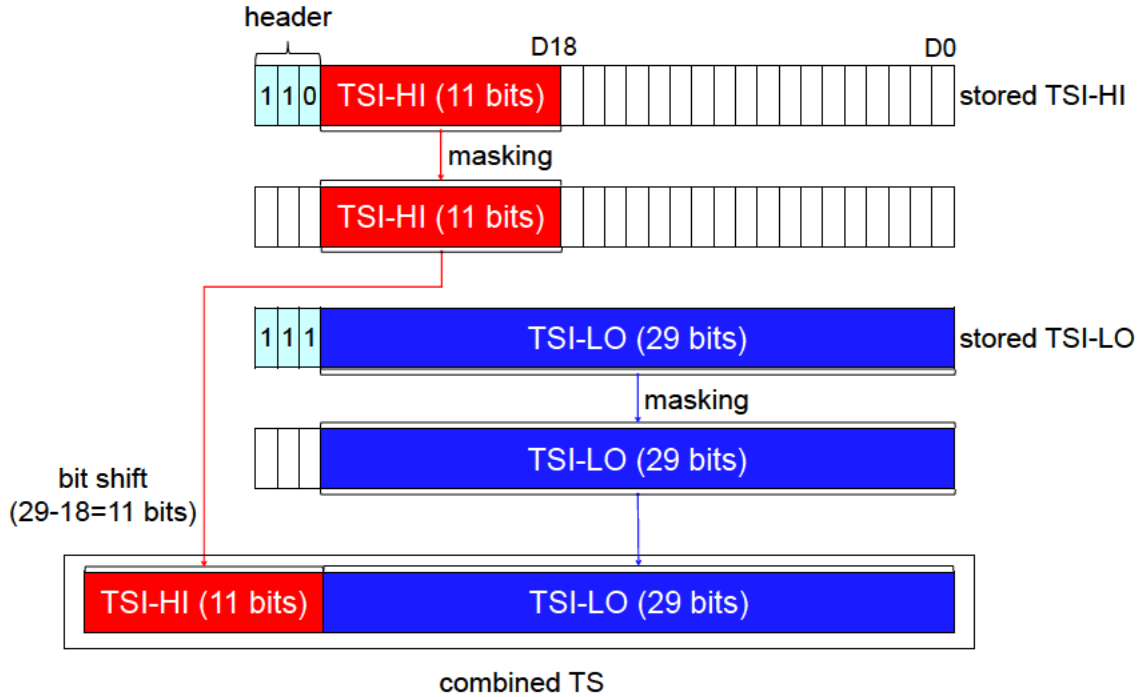


Figure 3.3: Time Stamps stored in A3400 VME module.

tester was operated for almost 10 minutes about every 10 seconds as shown in Figure 3.2. Therefore, to synchronize both the data obtained by the DAQ and VLSI tester, it is required to obtain the time information of the DAQ and muon fluence in the VLSI operation period.

The time information of the DAQ was registered in A3400 VME module as Time Stamps (TSs). A3400 VME module stored the data obtained in this experiment in total 40 bits for each storage channel and the 3 bits at the head represent the types of data as header. A TS has the minimum measurement time of 5 nsec per a bit and consists of 11 bits Time Stamp Information-High (TSI-HI, header: '110') and 29 bits -Low (TSI-LO, header: '111'). TSI-HI and TSI-LO are stored in A3400 VME module as shown in Figure 3.3. In the experiment, the minimum measurement time was set to 100 ns. Therefore, '1' was input to the first digit of TSI-LO after the elapse of 100 ns from DAQ operation. Then, '1' was input to the first digit of TSI-HI after the elapse of 100 ns from the state where 29 bits of TSI-HI is filled with '1'. Each bit of TSI-HI needs to be shifted to the left by 11 bits when combining with TSI-LO since the end of TSI-HI must be attached to the beginning of TSI-LO and TSI-HI starts from the 18th digit (D18).

## 3.2 Analysis of Muonic X-rays

In the experiment, muonic X-rays were detected by Ge detectors. The data analysis for muonic X-rays is described below.

### 3.2.1 Standard source measurement

In the experiment, the Ge detectors were used to detect muonic X-rays emitted from the irradiated device board. When a photon enters to the Ge crystal, ADC channel value corresponding to the deposited charge is recorded. To identify the types of muonic X-rays, it is necessary to calibrate the ADC channel value to the energy. In addition, since the detection efficiency of the Ge detector depends on the energy of the detected particle, it is necessary to derive the detection efficiency as a function of energy. In the experiment, several standard  $\gamma$ -ray sources were used for energy calibration and deriving the detection efficiency. The standard sources used in the experiment are listed in Table 3.1 with the radioactivity on the day of the present experiment  $A_\gamma$ , the uncertainty of radioactivity  $\Delta A_\gamma$ , the energy of  $\gamma$ -ray in units of [keV]  $E_\gamma$  and the branch ratio  $R_\gamma$ . Each spectrum of  $\gamma$ -ray from sources was fitted with the following

Table 3.1: Standard sources used in the experiment

source	$A_\gamma$ [kBq]	$\Delta A_\gamma$ [%]	$E_\gamma$ [keV]	$R_\gamma$ [%]
$^{152}\text{Eu}$	292.1	1.9	121.8	28.58
			244.7	7.58
			295.9	0.45
			344.3	26.50
			367.8	0.86
			411.1	2.23
			444.0	2.82
			778.9	12.94
			867.4	4.26
			964.1	14.61
$^{133}\text{Ba}$	321.6	1.8	53.2	2.12
			81.0	34.06
			160.6	0.65
			223.2	0.45
			276.4	7.16
			302.9	18.33
			356.0	62.05
			383.9	8.94

expression combining a Gaussian and a linear function:

$$f(C_{\text{Ge}}) = p_0 \exp\left(\frac{-(C_{\text{Ge}} - p_1)^2}{2p_2^2}\right) + p_3 C_{\text{Ge}} + p_4, \quad (3.5)$$

where  $p_{0-4}$  are the fitting parameters and  $C_{\text{Ge}}$  is the ADC channel value. The first term (Gaussian part) represents the detected  $\gamma$ -ray spectrum, and the second and third ones (linear part) represent the background component. An example of the  $\gamma$ -ray spectrum fitted by Eq. (3.5) is shown in Figure 3.4.  $p_{0-2}$  obtained from the fitting result were used to make the energy calibration and derive the detector efficiency for Ge detector.

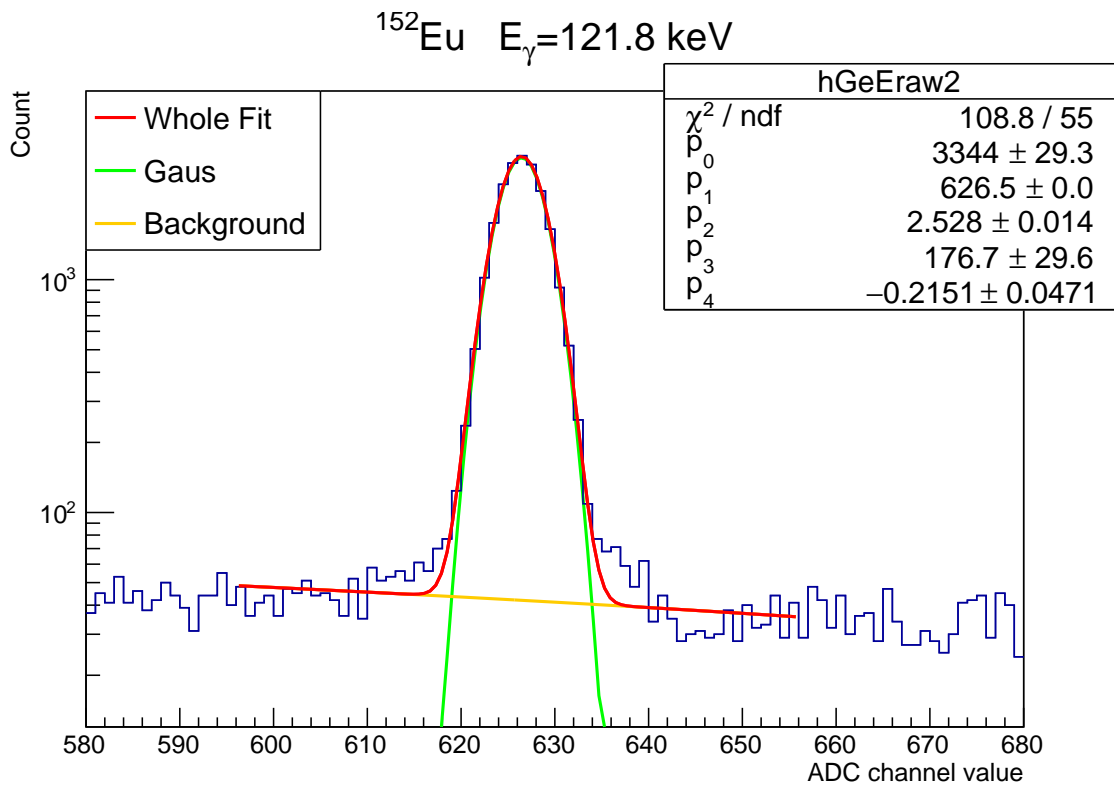


Figure 3.4: An example of fitting for  $\gamma$ -ray with energy 121.8 keV from  $^{152}\text{Eu}$ . The red line (Whole Fit) represents the fitting result according to Eq. (3.5). The green (Gaus) and yellow (Background) ones represent the Gaussian and linear part in Eq. (3.5), respectively.

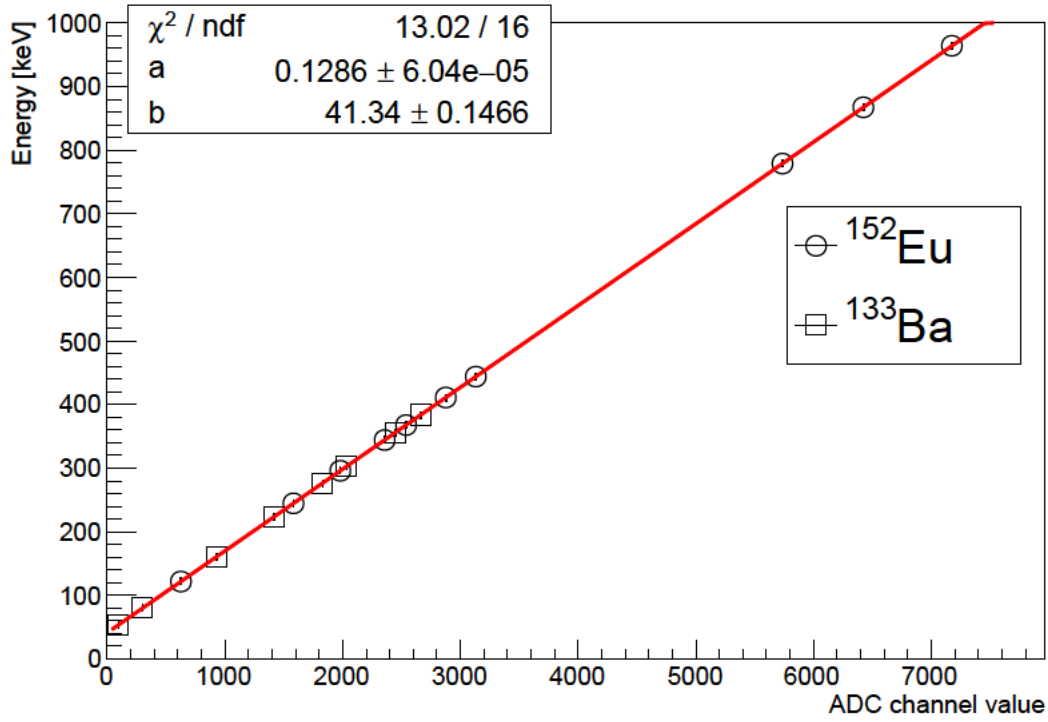


Figure 3.5: Energy calibration line for Ge detector with points which represent the energy and ADC channel value of  $\gamma$ -rays from the standard sources,  $^{152}\text{Eu}$  and  $^{133}\text{Ba}$ .

### 3.2.2 Energy calibration

For energy calibration of the Ge detectors, it is necessary to derive the relationship between the ADC channel value ( $C_{\text{Ge}}$ ) and the energy of  $\gamma$ -rays ( $E_{\text{Ge}}$ ). The following linear function was used to describe the relationship between  $C_{\text{Ge}}$  and  $E_{\text{Ge}}$ :

$$E_{\text{Ge}} = q_0 C_{\text{Ge}} + q_1, \quad (3.6)$$

where  $q_{0,1}$  are the fitting parameters. Then, the fitting result using Eq. (3.6) is shown in Figure 3.5.

### 3.2.3 Detection efficiency

In general, the detection efficiency of Ge detectors has a constant value from 20 to 100 keV and decreases exponentially thereafter. In this study, the data analysis of silicon  $\text{K}\alpha$  muonic X-rays with the energy 400.3 keV is necessary to derive the stopping number of muons in silicon in the irradiated board. Therefore, the detection efficiency of Ge detector in the energy range from 100 to 1000 keV was derived using the standard sources. Firstly, the detection efficiency for each  $\gamma$ -ray from the standard sources was obtained by the following equation:

$$\epsilon_\gamma = \frac{\sqrt{2\pi} p_0 p_2}{A_\gamma (R_\gamma / 100) t}, \quad (3.7)$$

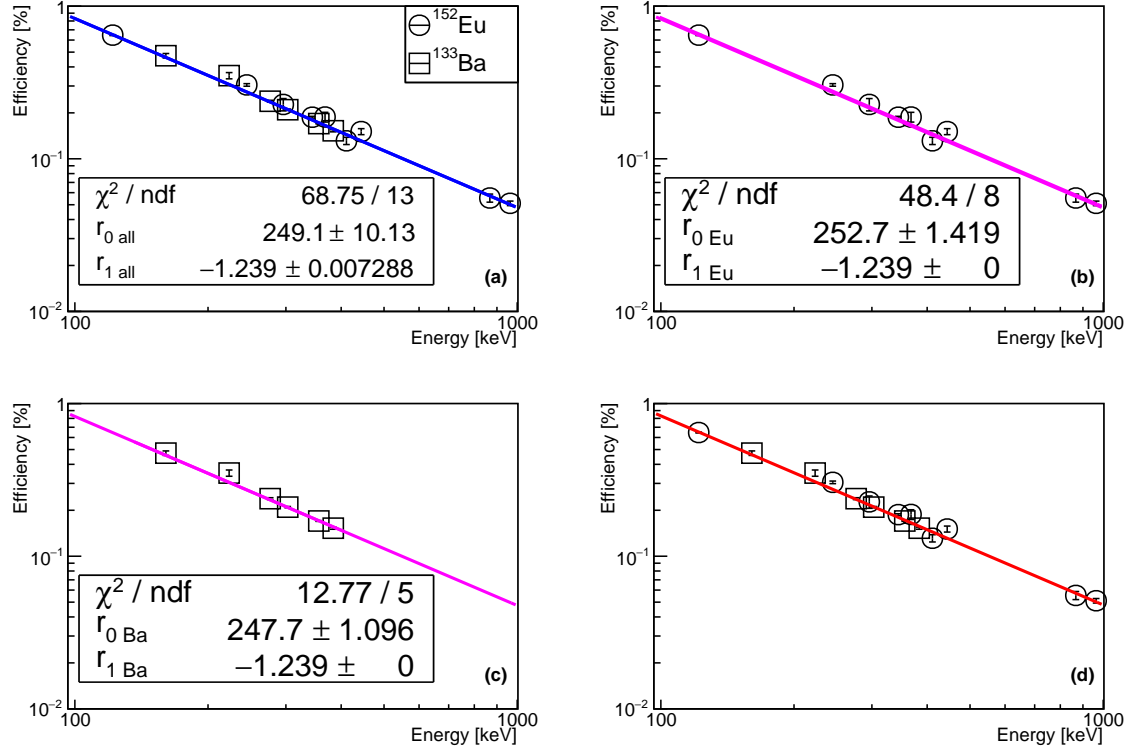


Figure 3.6: Fitting result for the detection efficiency for the  $\gamma$ -rays from the standard sources ((a),(b) and (c)) and the finally obtained efficiency function with the equation  $\epsilon(E_{\text{Ge}}) = r_0 E_{\text{Ge}}^{r_1}$  at  $r_0 = 249.9$  and  $r_1 = -1.239$ .

where  $t$  is the measurement time for each standard source. The numerator of Eq. (3.7) represents the number of detected  $\gamma$ -rays derived by Gaussian integral by using parameters  $(p_{0,2})$  in the formula of Eq. (3.5). The denominator represents the total number of emitted  $\gamma$ -rays from the standard sources in the time period of  $t$ . Secondly, the efficiencies derived by Eq. (3.7) were fitted by the following equation:

$$\epsilon(E_{\text{Ge}}) = r_0 E_{\text{Ge}}^{r_1}, \quad (3.8)$$

where  $r_{0,1}$  are the fitting parameters. The result of fitting using Eq. (3.8) is shown in Figure 3.6-(a) and let  $r_{0,1}$  obtained here be  $r_{0,1\text{all}}$  and their uncertainties be  $\Delta r_{0,1\text{all}}$ . Thirdly,  $r_{1\text{all}} (= -1.239)$  from the above fitting result as shown in Figure 3.6-(a) was fixed and the detection efficiency of  $\gamma$ -rays from each of  $^{152}\text{Eu}$  and  $^{133}\text{Ba}$  were fitted by Eq. (3.8) again, respectively. The result of fitting is shown in Figure 3.6-(b) and (c) and let  $r_0$  obtained here be  $r_{0\text{Eu}}$  and  $r_{0\text{Ba}}$  and their uncertainties obtained by fitting be  $\Delta r_{0\text{Eu}}$  and  $\Delta r_{0\text{Ba}}$ , respectively. Finally,  $r_0$  was derived by averaging  $r_{0\text{Eu}}$  and  $r_{0\text{Ba}}$  in the following equation:

$$r_0 = \frac{r_{0\text{Eu}} \times (\Delta r_{0\text{Ba}} (A_{\gamma\text{Ba}}/100))^2 + r_{0\text{Ba}} \times (\Delta p_{0\text{Eu}} (A_{\gamma\text{Eu}}/100))^2}{\Delta r_{0\text{Eu}}^2 + \Delta r_{0\text{Ba}}^2}, \quad (3.9)$$

where  $A_{\gamma\text{Eu}}$  and  $A_{\gamma\text{Ba}}$  are the uncertainties of radioactivity for  $^{152}\text{Eu}$  and  $^{133}\text{Ba}$ , respectively. Then,  $r_0 = 249.9 \pm 4.1$  was obtained from (3.9). The finally obtained efficiency is shown in Figure 3.6-(d).

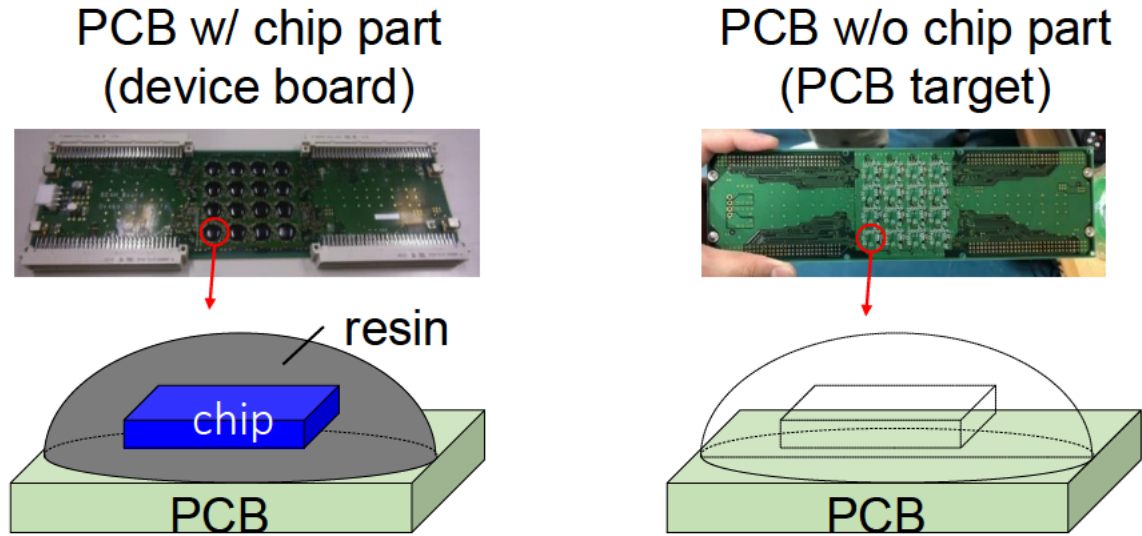


Figure 3.7: Schematic illustration of a PCB target compared with device board.

### 3.2.4 Identification of muonic X-rays generation positions

In the study, we focused on muonic X-rays from Si because SRAM chips consist of silicon. Since PCB also contains a large amount of Si as in the SRAM chips and resin (hereinafter referred to as a chip part), additional irradiation tests of the PCB without the chip part (hereinafter referred to as a PCB target), as shown in Figure 3.7, were performed in order to estimate the contribution of muonic X-rays from Si in the PCB.

The muonic X-ray spectra from the device board and PCB are shown in Figure 3.8. The difference can be observed between the spectra from the device board and PCB. In addition, the spectra with the range from 50 keV to 150 keV is shown in Figure 3.9. There are some muonic X-rays from atoms in the device board and PCB. It is important to consider the effects of boron in neutron-induced SEUs since  $\alpha$  particles are emitted through the reaction  $^{10}\text{B}(n, \alpha)^7\text{Li}$  with thermal neutrons. Carbon and oxygen are major elements contained in the device board. However, oxygen is also contained in air as well as nitrogen, therefore, it is difficult to identify whether the muonic X-rays emitted from the device board or air.

The energy spectrum of silicon  $K\alpha$  muonic X-rays measured under irradiation of the 36.6-MeV/c negative muon beam for the device board and the PCB alone are shown in Figure 3.10. The detection counts of the X-rays are normalized by the number of incident muons. The peaks around 400 keV are observed in both the device board and PCB. The peak counts in the PCB case are less than those in the device board case. By subtracting the former counts from the latter ones, the emission rate of silicon  $K\alpha$  muonic X-rays from the chip part including the chip and resin per incident muon was derived.

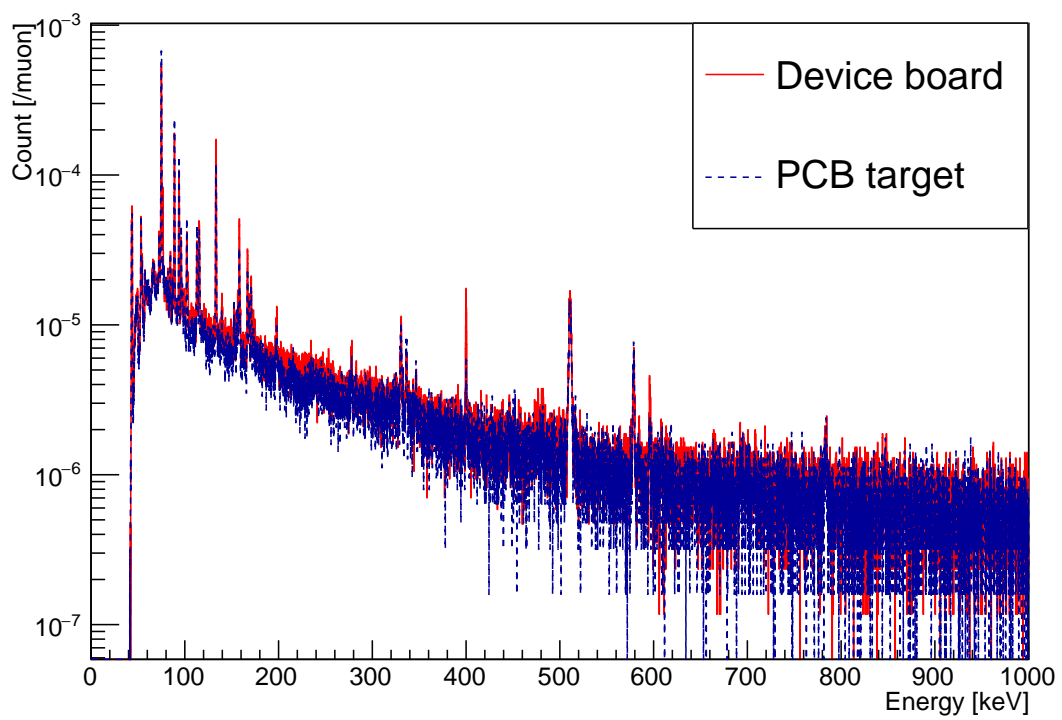


Figure 3.8: Comparison of energy spectra of muonic X-rays from device board and PCB target.

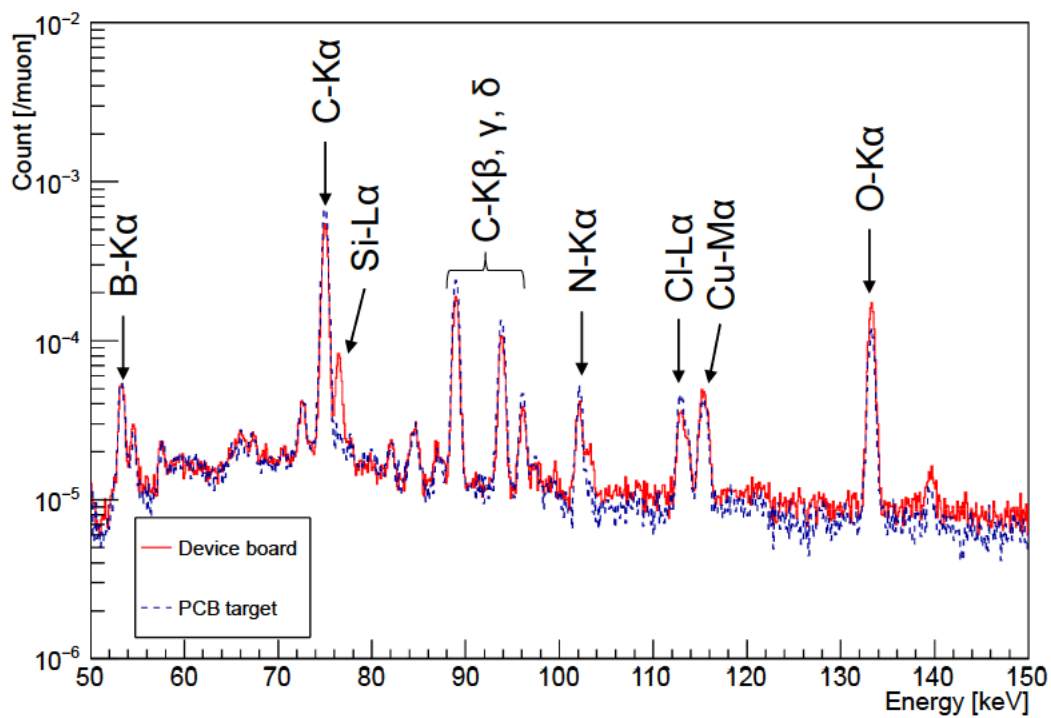


Figure 3.9: Comparison of energy spectra of muonic X-rays from device board and PCB target in the range of 50 keV~150 keV.

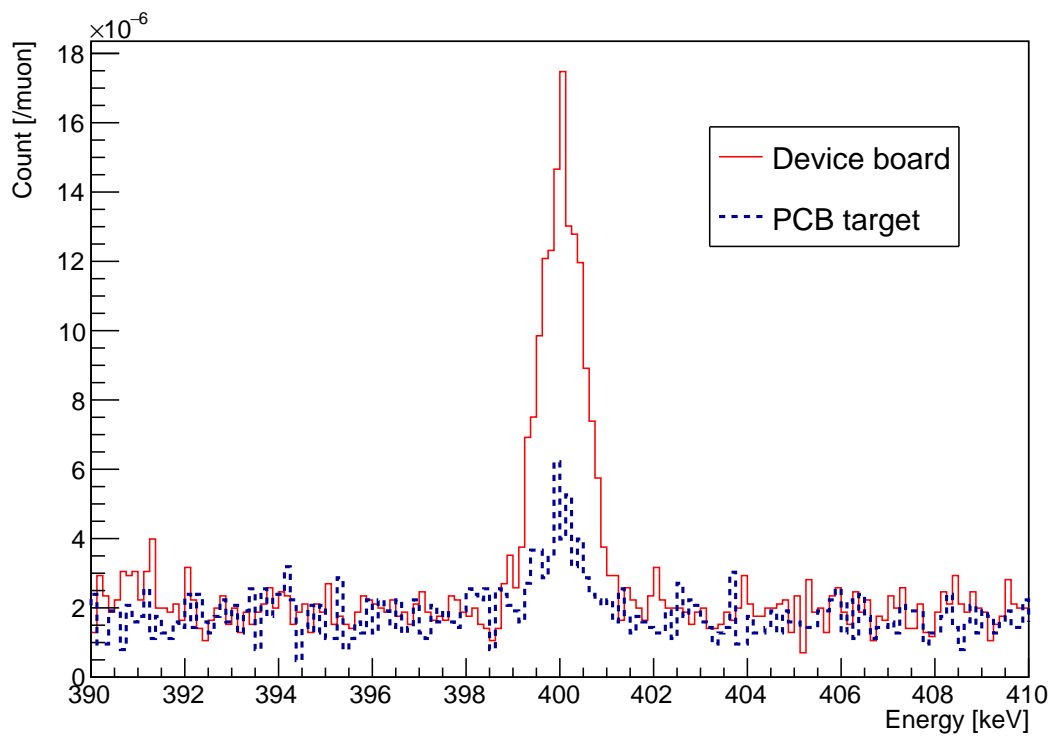


Figure 3.10: The energy spectra of muonic X-rays emitted from the device board (red solid line) or the PCB alone (blue dot line). The incident muon incident momentum is 38.9 MeV/c at beam exit. The energy of silicon  $K\alpha$  muonic X-ray is about 400 keV.

# Chapter 4

## Experimental Results and Discussion

### 4.1 SEU Cross Section

#### 4.1.1 Background run

To estimate the probability of SEUs induced by background radiation (e.g., thermal neutrons and  $\gamma$ -rays), another device board was operated for monitoring under the base plate on which the irradiated device board was set as a reference board. The result showed that the number of errors observed in the reference board was less than 2% of that in the irradiated device. In addition, another 5-mm-thick aluminium plate was placed between the forward PS and the device board. In this case, all negative muons were fully stopped in the aluminium plate before entering the device board, and various kinds of generated radiation other than muons (i.e., decay electrons, neutrons,  $\gamma$ -rays, etc.) bombarded the device board. As a result, no SEU was observed under this situation. Thus, it was confirmed that the probability of SEU induced by background radiations was negligible.

#### 4.1.2 Momentum and operating voltage dependence

The negative muon SEU cross sections were measured as a function of incident muon momentum. Since both the experiments were performed in different irradiation configurations as shown in Figure 4.1, the momentum just before the muons enter the device board is used for comparison of both the experimental results in the present work. Note that the incident momentum at the beam exit was used in the literature of our previous MUSE experiments [14], [15]. The momentum was estimated by the energy loss simulation with PHITS [26] for both the cases. Two examples of the simulation are shown in Figure 4.2 and 4.3. The momentum distribution can be approximated by a normal distribution with the standard deviation of 9.6% at MuSIC and 5.9% at MUSE respectively for the incident momentum of 35.3 MeV/c and 35.4 MeV/c, which corresponds to 7.0% and 5.0% at the beam exit.

Since the muon beam has a momentum distribution, the measured SEU cross section represents the averaged value over the momentum distribution,  $\langle\sigma_{\text{SEU}}(p)\rangle$ , which is

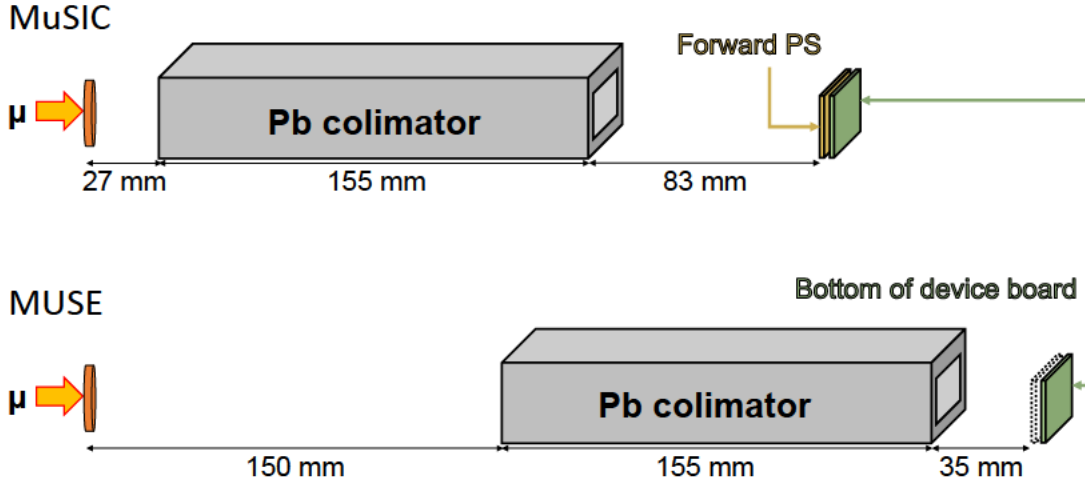


Figure 4.1: Comparison of the experimental setup at MuSIC and MUSE. There are three differences between them; the shape of the muon beam (Gaussian-distribution of  $\sigma_x = \sigma_y = 21$  mm at MuSIC and square of  $x = y = 10$  mm at MUSE), distance among the beam exit, collimator and device board and whether the forward PS was used or not. In PHITS simulation, the momentum distribution in the bottom of the device board at MuSIC and MUSE was calculated.

defined by the following expression:

$$\langle \sigma_{\text{SEU}}(p) \rangle = \frac{\int_0^{\infty} \sigma_{\text{SEU}} \times \phi(p, p_{\text{mean}}) dp}{\int_0^{\infty} \phi(p, p_{\text{mean}}) dp}, \quad (4.1)$$

where  $p_{\text{mean}}$  represents the mean momentum in the momentum distribution,  $\sigma_{\text{SEU}}(p)$  is the mono-momentum muon SEU cross section at the momentum  $p$  and  $\phi(p, p_{\text{mean}})$  is the fluence of incident muons with the momentum  $p$  in the case of muon irradiation with the mean momentum  $p_{\text{mean}}$ .

The measured SEU cross sections are plotted as a function of incident muon momentum and compared with the previous measurement with MUSE pulse beams [14], [15] in Figure 4.4. The error bars show only the statistical uncertainties. There was no noticeable difference between the measured SEU cross sections at MuSIC and those at MUSE. However, the magnitude is slightly different between them. It could be partially caused by the difference in the momentum distribution between MUSE and MuSIC beams. When a muon stops near the SV, it can deposit the maximum charge because of the Bragg peak and/or the negative muon capture reaction as mentioned in [7], [13] and [14]. In the present test condition, muons with the momentum of about 36 MeV/c seem to be able to stop near the SVs because both the momentum dependence of SEU cross sections in MUSE and MuSIC have peaks around 36 MeV/c. The MuSIC beam has a larger standard deviation than the MUSE beam as mentioned before. This indicates that the ratio of 36-MeV/c muons to total muons in MuSIC is smaller than that in MUSE. Thus, we believe that the momentum dependence measured in the present work is in good agreement with that in the previous work. To investigate

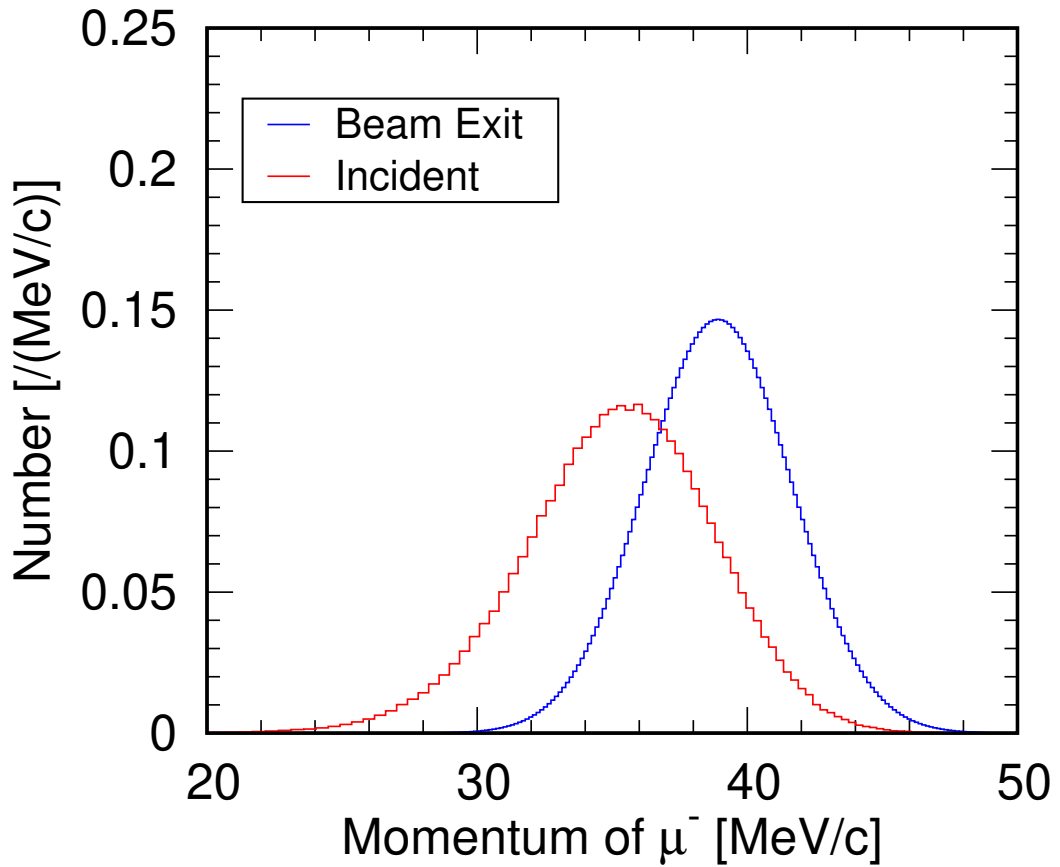


Figure 4.2: Result of the loss energy simulation by PHITS in the case of MuSIC at the mean of incident momentum of 38.9 MeV/c. The “Beam Exit” and “Incident” represents the momentum distribution at the beam exit and before the device board, respectively.

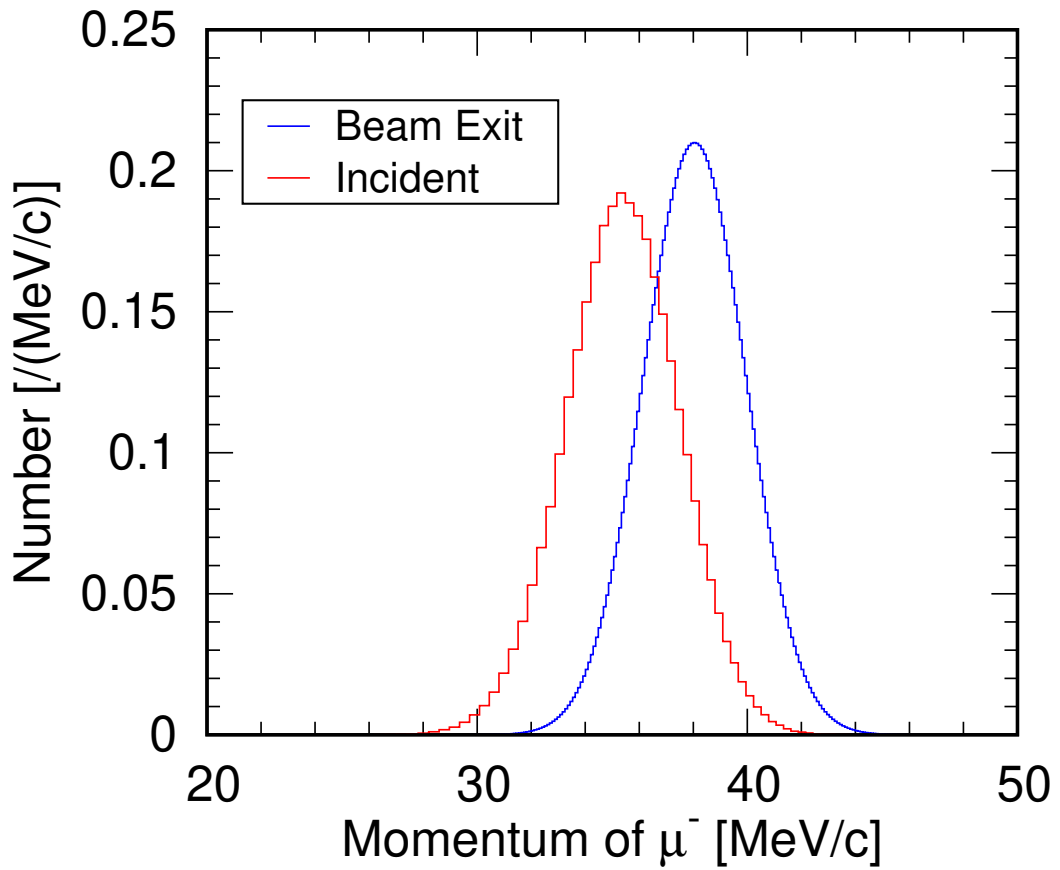


Figure 4.3: Result of the loss energy simulation by PHITS in the case of MuSE at the mean of incident momentum of 37 MeV/c.

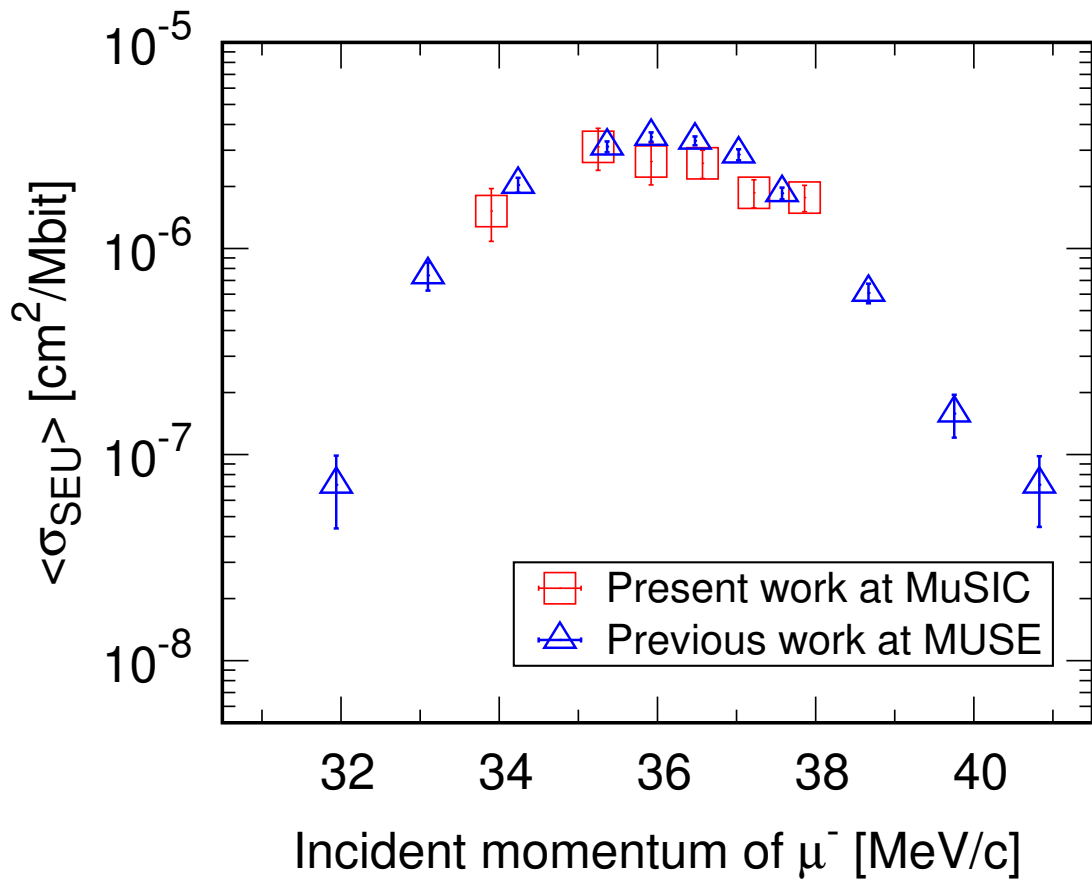


Figure 4.4: Comparison of the incident momentum dependence of the negative muon-induced SEU cross sections measured at MuSIC and MUSE. The data at MUSE was obtained from [14], [15]. The SRAM chips were operated at the voltage of 0.9 V.

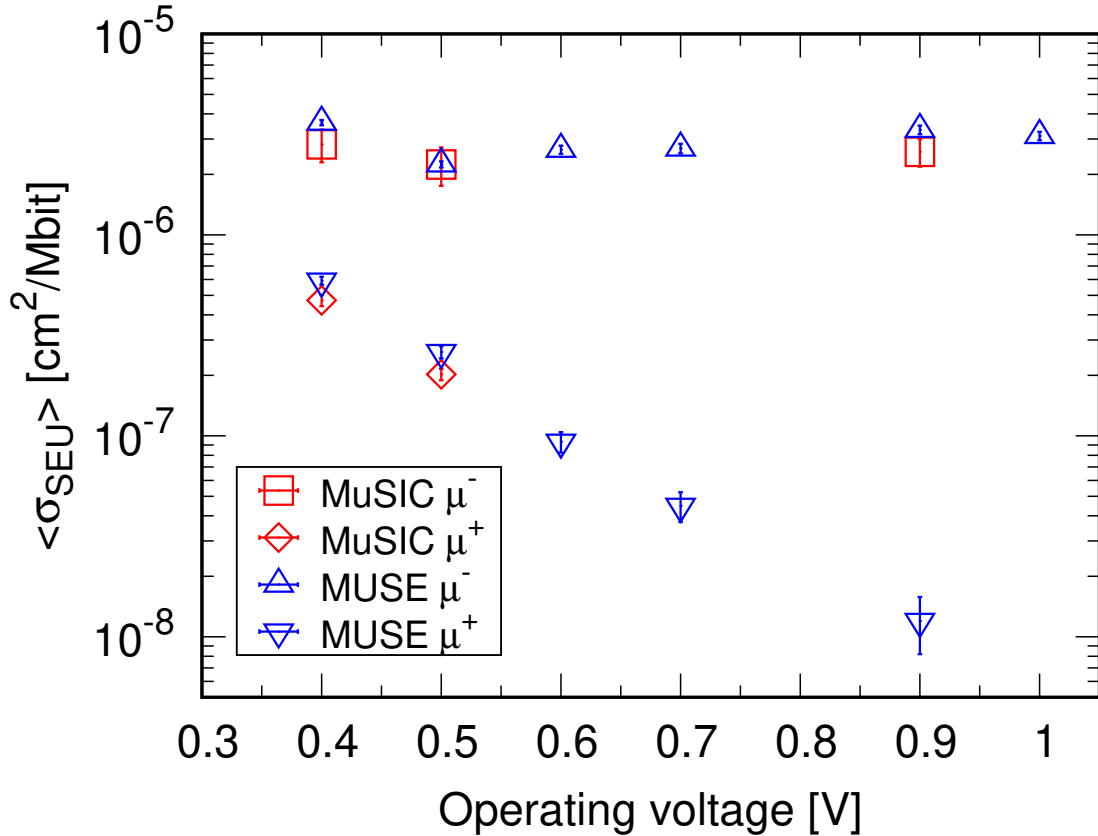


Figure 4.5: Comparison of the operating voltage dependence of the negative and positive muon-induced SEU cross sections measured at MuSIC and MUSE. The data at MUSE was obtained from [15], [17]. The means of momentum of muons are 36.6 MeV/c at MuSIC and 36.5 MeV/c.

the difference of between the SEU cross sections obtained at MuSIC and MUSE, the SEU simulation was performed and is discussed in Chapter 5.

The negative and positive muon-induced SEU cross section for the SRAMs measured at the operating voltage of 0.4 and 0.5 V are shown in Figure 4.5. The SRAMs operated at the voltage of 0.9 V was not irradiated by the positive muon beam because the lower error rate requires longer test time to obtain the sufficient statistics. On the other hand, 0.4 and 0.5 V was selected as the operating voltage to measure positive muon induced SEU cross sections because short measurement time is required to obtain the sufficient statistics. The voltage dependence shows a good agreement with that observed in the previous work [14], [15], as the momentum dependence does in Figure 4.4. The negative-muon SEU cross sections are about 6 and 11 times larger than the positive-muon ones in the case of 0.4- and 0.5-V operating voltages, respectively.

## 4.2 Muonic X-ray

The relation among the emission rate from the chip part, the emission rate from the PCB, and the negative muon SEU cross section is plotted as a function of incident

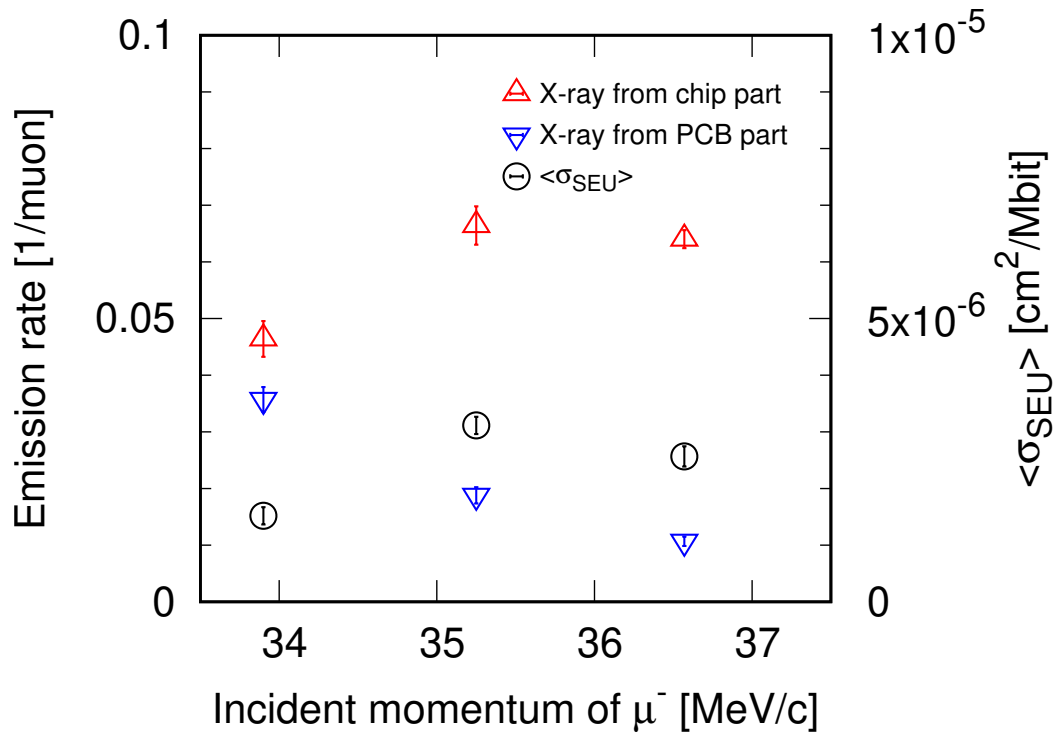


Figure 4.6: The relationship between the emission rate of muonic X-rays from chips or resin and the negative muon SEU cross section. The SEU cross section was measured for the 65-nm bulk SRAMs at the operating voltage of 0.9 V.

muon momentum in Figure 4.6. The measured emission rate of silicon  $K\alpha$  muonic X-rays from the chip part increases as the momentum of the incident negative muons increase while that from the PCB decreases. This trend indicates that the number of muons penetrating the PCB and reaching the chip part increases as the momentum of the incident muon increases. Furthermore, the measured emission rate of  $K\alpha$  muonic X-rays from the chip part shows the momentum dependence similar to that of the SEU cross sections. The intensity of the muonic X-rays is proportional to the number of stopping muons that are captured by silicon atoms in the chip part. Therefore, this experimental result suggests that the number of negative muons stopped near the SVs in SRAMs has a positive correlation with the occurrence of SEUs.

# Chapter 5

## Simulation

The simulation of muon induced SEU and muonic X-rays was carried out to analyze the experimental result. In this section, the simulation method and comparison result with the experiment result are described.

### 5.1 Method

The simulation was performed based on the sensitive volume (SV) model [33] using the simulation with PHITS ver 3.00 [26]. PHITS is a general purpose Monte-Carlo particle transport simulation code developed by Japan Atomic Energy Agency (JAEA). PHITS has been used in recent simulation muon-induced soft error [14], [16]. Here, the model and configuration used in the simulation are described below.

#### 5.1.1 Sensitive volume model

In the SV model, the sensitive volume is defined in each SRAM cell. All charge deposited in an SV is assumed to be collected to the drain node without device simulation. An SEU is assumed to occur when the total charge deposited in the defined SV exceeds the critical charge  $Q_c$ . In the PHITS simulation, the deposited energy in SV was calculated. The minimum energy to generate an electron-hole pair is 3.6 eV in silicon. Hence, the deposited charge  $q$  is calculated based on this value by the following equation:

$$q = \frac{e}{3.6 \times 10^{-6} [\text{MeV}]} \cdot E_d, \quad (5.1)$$

where  $e$  represents the elementary charge ( $= 1.602 \times 10^{-19}$  C) and  $E_d$  represents the deposited energy in the SV in units of [MeV].

#### 5.1.2 Simulation procedure

The SEU simulation was performed with the method described in [14], [16]. The purpose of the SEU simulation is to demonstrate that the difference between the SEU cross sections measured at two facilities is caused by the difference between the momentum distribution of negative muons.

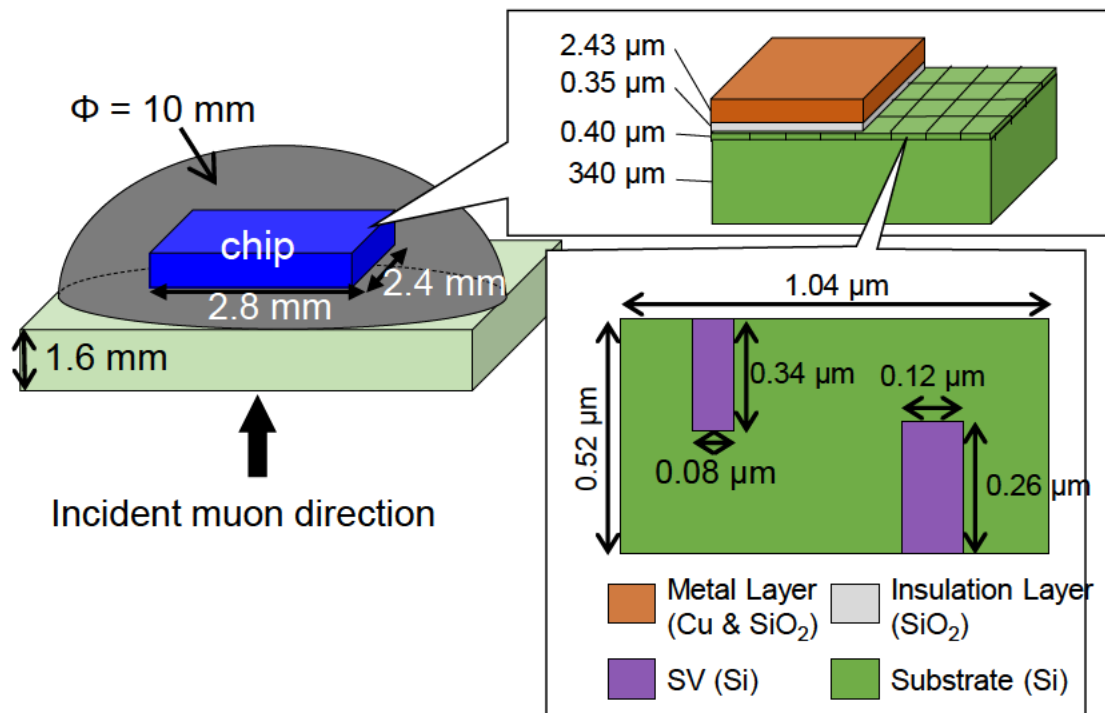


Figure 5.1: The Configuration of a single chip used in PHITS simulation. 12-Mbit SRAMs are placed on a chip.

A single chip illustrated in Figure 5.1 was irradiated by negative muons with momentum distribution calculated in Section 4.1. The chip consists of 12-Mbits SRAM cells whose size is  $1.04 \mu\text{m} \times 0.52 \mu\text{m} \times 0.012 \mu\text{m}$  on a  $300\text{-}\mu\text{m}$ -thick Si substrate. The SV of the SRAM cell is defined as the source and drain region, and the region with thickness of  $0.4 \mu\text{m}$  under the gate of the nMOSFET and pMOSFET with the state of “OFF”. Then, the deposit energy in the SV by muon and secondary particles emitted via the negative muon capture reaction was calculated. The inner structure of the chip is depicted schematically in Figure 5.1.

Next, the emission rate of muonic X-rays from the chip part  $R_{\text{chip part}}$  were predicted by calculating the number of muons stopping in chips and resins on the simulation and using the following equation:

$$R_{\text{chip part}} = \frac{(N_{\text{stop in chip}} + N_{\text{stop in resin}} \cdot \epsilon_{\text{Si in resin}}) \cdot \epsilon_{\text{Si-K}\alpha}}{N_{\text{muon}}}, \quad (5.2)$$

where  $N_{\text{stop in chip}}$  and  $N_{\text{stop in resin}}$  are the numbers of muons stopping in chips and resins, respectively,  $\epsilon_{\text{Si in resin}}$  represents the probability on which a muon stopped in resins is captured in silicon,  $\epsilon_{\text{Si-K}\alpha}$  represents the probability on which a muon captured in silicon emits a  $\text{K}\alpha$  muonic X-ray and  $N_{\text{muon}}$  represents the number of incident muons. The resin consists of Si, C and O with the comparison ratio of Si : C : O = 1 : 1.65 : 2.41.  $\epsilon_{\text{Si in resin}}$  is roughly calculated by the following equation:

$$\begin{aligned} \epsilon_{\text{Si in resin}} &= \frac{C_{\text{Si}} \cdot M_{\text{Si}}}{C_{\text{Si}} \cdot M_{\text{Si}} + C_{\text{C}} \cdot M_{\text{C}} + C_{\text{O}} \cdot M_{\text{O}}} \\ &= \frac{1 \times 28}{1 \times 28 + 1.65 \times 12 + 2.41 \times 16}, \end{aligned} \quad (5.3)$$

where  $C_{\text{Si}, \text{C}, \text{O}}$  and  $M_{\text{Si}, \text{C}, \text{O}}$  represent the comparison ratios and mass numbers of Si, C and O, respectively. The value of  $\epsilon_{\text{Si-K}\alpha}$  was 0.792 from [34].

## 5.2 Simulation Result

### 5.2.1 SEU simulation

The simulation result is compared with the experimental result as shown in Figure 5.2. Note that the  $Q_c$  in the simulation was chosen as 1.5 fC and the simulated cross section at MUSE with the irradiation momentum of  $36.5 \text{ MeV}/c$  is normalized to measured one. The reference [16] reported that the PHITS-SV simulation reproduces the negative muon-induced SEU cross sections measured at MUSE generally well. The method chooses  $Q_c$  so as to reproduce the ratio of the negative and positive muon cross sections and normalizes the simulated cross section to experimental one at the momentum where the cross section has a peak. Hence, the same simulation method are applied to analyze the experimental result at MuSIC. The result shows that the experimental and simulated cross sections of MuSIC match within the statistical uncertainties except at  $35.3 \text{ MeV}/c$ . Moreover, the simulation reproduce the difference between SEU cross sections measured at MuSIC and MUSE. The difference of the simulation for two facilities is only the momentum distribution. Thus, the result demonstrate that the difference between SEU cross sections was caused by the difference in momentum.

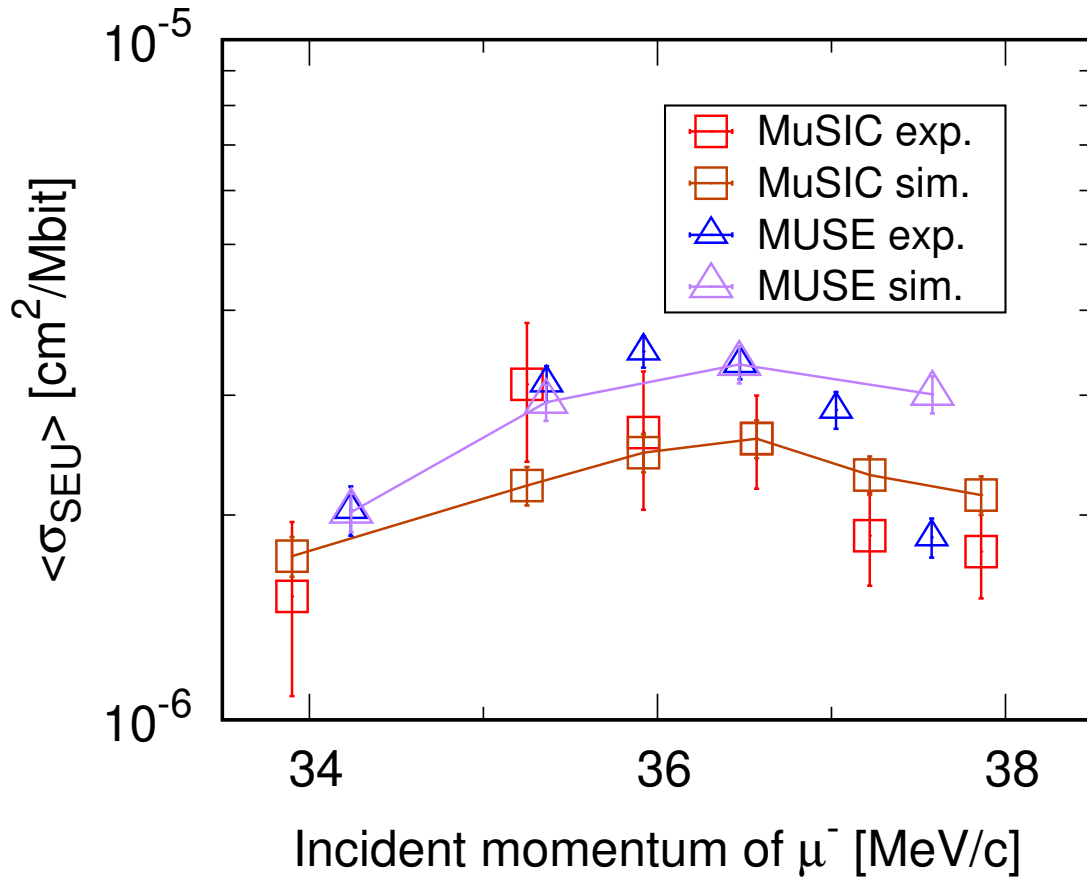


Figure 5.2: Comparison of the SEU cross sections simulated by PHITS with the experimental result obtained in the present work at MuSIC and previous work at MUSE.

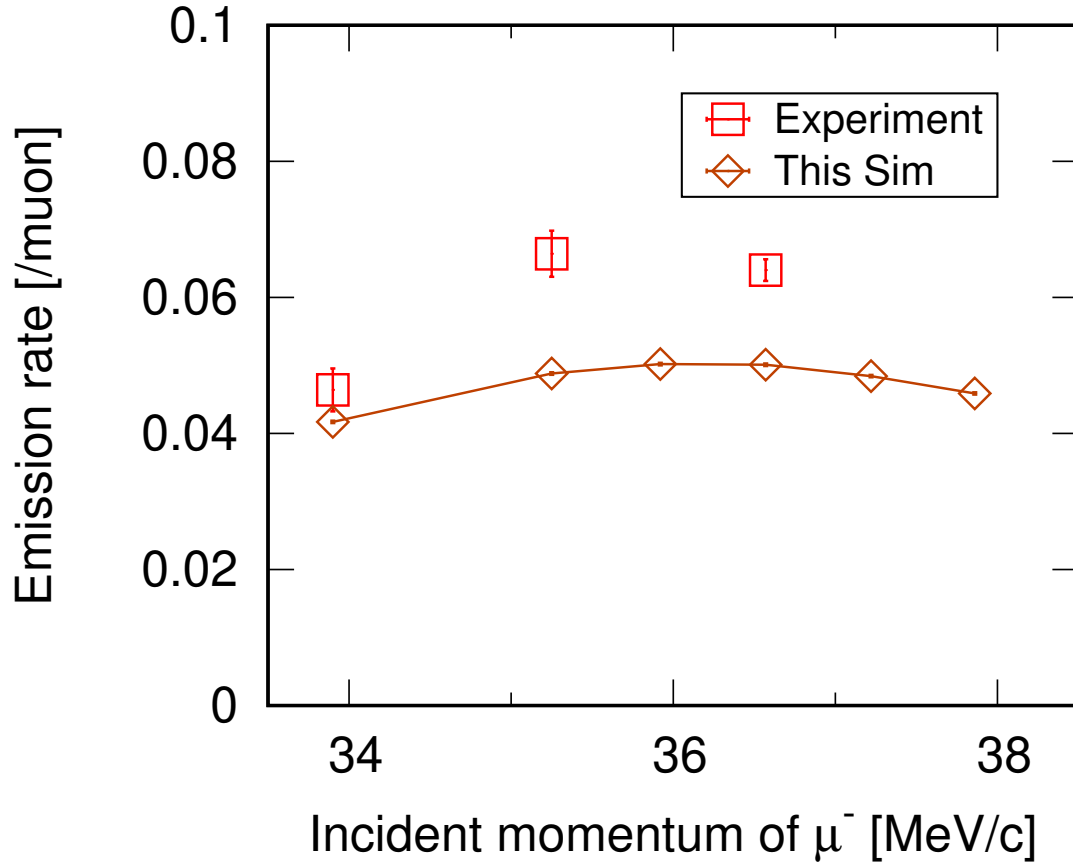


Figure 5.3: Comparison of the emission rate of muonic X-rays from chip part simulated by PHITS with the experimental result obtained in the present work at MuSIC.

### 5.2.2 Muonic X-ray simulation

The result of muonic X-ray simulation is compared with the experimental one in Figure 5.3. The simulation result generally agrees with the experimental result within 30%. The difference seems to be caused by the uncertainty of the device structure, mainly the detail of its elemental composition. Therefore, it is necessary to reveal the inner structure of the device using a destructive way for more accurate muonic X-ray simulation.

# Chapter 6

## Summary and Conclusion

We have conducted an irradiation test for the 65-nm bulk SRAMs with the DC muon beams at RCNP-MuSIC facility. The incident muon fluence was measured one by one using a plastic scintillator by taking an advantage of the DC beam with the systematic error only 2%. Thus, reliable absolute values of SEU cross sections were successfully determined. The measured negative and positive muon SEU cross sections showed a good agreement with those measured in the MUSE facility [14], [15]. Thus, the previous MUSE result was validated by the present MuSIC result. Moreover, our present and past works demonstrated that two muon facilities in Japan are available for muon irradiation tests of memory devices.

In addition to the cross section measurement, the energy spectra of muonic X-rays were measured to investigate the muon stopping position in the irradiated device. The positive correlation between the SEU cross section and the emission rate of muonic X-rays from the SRAM chips or resins was clearly observed. The X-ray measurement demonstrated the importance of the stopping negative muon, i.e., the negative muon capture reaction, near the sensitive volume on the occurrence of SEUs, which was suggested by the simulation in [14].

Furthermore, the PHITS simulation of SEUs and muonic X-rays were performed. The SEU simulation shows that the difference between SEU cross sections measured at MuSIC and MUSE is reasonable in consideration of the difference of muon momentum distribution, so that the validity of the previous work was also confirmed by the PHITS simulation. In addition, the emission rate of muonic X-rays calculated by PHITS simulation roughly agrees with the experimental emission rate, however, a small discrepancy was observed.

For further quantitative discussion and understanding on the mechanism of the negative muon SEU, we plan to perform a muon transport and muonic X-rays simulation by considering the more realistic device board structure, and compare the simulation and the present experimental result to validate the simulation code. By using the validated simulation code, we are going to investigate the mechanism of muon-induced SEU in details, e.g., the relation among the stopping muon position, the species of the ions emitted via negative muon capture reaction on the atomic nuclei at the stopping position, and the SEU occurrence probability.

# References

- [1] Ministry of Internal Affairs and Communications homepage. <https://www.soumu.go.jp/johotsusintokei/whitepaper/ja/r01/html/nd112120.html>.
- [2] G. E. Moore, "Cramming more components onto integrated circuit," *Electronics*, vol. 19, no. 8, 1965.
- [3] T. Sato, EXPACS." <https://phits.jaea.go.jp/expacs/jpn.html>.
- [4] T. Sato, "Analytical Model for Estimating Terrestrial Cosmic Ray Fluxes Nearly Anytime and Anywhere in the World: Extension of PARMA/EXPACS," *PLoS ONE*, vol. 10, no. 12, pp. 1–33, 2015.
- [5] T. Sato, "Analytical Model for Estimating the Zenith Angle Dependence of Terrestrial Cosmic Ray Fluxes," *PLoS ONE*, vol. 11, no. 8, pp. 1–22, 2016.
- [6] B. D. Sierawski, M. H. Mendenhall, R. A. Reed, M. A. Clemens, R. A. Weller, R. D. Schrimpf, E. W. Blackmore, M. Trinczek, B. Hitti, J. A. Pellish, R. C. Baumann, S. Wen, R. Wong, and N. Tam, "Muon-Induced Single Event Upsets in Deep-Submicron Technology," *IEEE Transactions on Nuclear Science*, vol. 57, no. 6, pp. 3273–3278, 2010.
- [7] B. D. Sierawski, R. A. Reed, M. H. Mendenhall, R. A. Weller, R. D. Schrimpf, S. Wen, R. Wong, N. Tam, and R. C. Baumann, "effects of scaling on muon-induced soft errors", in *Proc. 2011 International Reliability Physics Symposium (IRPS)*, 2011, pp. 3C.3.1–3C.3.6.
- [8] B. D. Sierawski, B. Bhuvu, R. Red, N. Tam, B. Narasimham, K. Ishida, A. Hillier, M. Trinczek, E. Blackmore, S. Wen, and R. Wong, "Bias dependence of muon-induced single event upsets in 28 nm static random access memories," in *Proc. 2014 IEEE International Reliability Physics Symposium (IRPS)*, 2014, 2B.2.1–2B.2.5.
- [9] N. Seifert, S. Jahinuzzaman, J. Velamala, and N. Patel, "Susceptibility of planar and 3D tri-gate technologies to muon-induced single event upsets," in *Proc. 2015 IEEE International Reliability Physics Symposium (IRPS)*, 2015, pp. 2C.1.1–2C.1.6.
- [10] G. Gasiot, D. Soussan, J. Autran, V. Malherbe, and P. Roche, "Muons and thermal neutrons SEU characterization of 28nm UTBB FD-SOI and Bulk eSRAMs," in *Proc. 2015 IEEE International Reliability Physics Symposium (IRPS)*, 2015, pp. 2C.2.1–2C.2.5.

- [11] J. M. Trippe, R. A. Reed, B. D. Sierawski, R. A. Weller, R. A. Austin, L. W. Massengill, B. L. Bhuvu, K. M. Warren, and B. Narasimham, “Predicting the vulnerability of memories to muon-induced SEUs with low-energy proton tests informed by Monte Carlo simulations,” in *Proc. 2016 IEEE International Reliability Physics Symposium (IRPS)*, 2016, SE-6-1-SE-6-6.
- [12] M. Bagatin, S. Gerardin, A. Paccagnella, A. Visconti, S. Beltrami, M. Bertuccio, K. Ishida, C. D. Frost, A. Hillier, and V. Ferlet-Cavrois, “Muon-induced soft errors in 16-nm NAND flash memories,” in *Proc. 2016 IEEE International Reliability Physics Symposium (IRPS)*, 2016, pp. 5C-1-1-5C-1-5.
- [13] S. Serre, S. Semikh, J. Autran, D. Munteanu, G. Gasiot, and P. Roche, “Effects of Low Energy Muons on Electronics: Physical Insights and Geant4 Simulation,” in *Proc. 13th European Conference on Radiation and its Effects on Components and Systems (RADECS)*, 2012.
- [14] S. Manabe, Y. Watanabe, W. Liao, M. Hashimoto, K. Nakano, H. Sato, T. Kin, S. Abe, K. Hamada, M. Tampo, and Y. Miyake, “Negative and Positive Muon-Induced Single Event Upsets in 65-nm UTBB SOI SRAMs,” *IEEE Transactions on Nuclear Science*, vol. 65, no. 8, pp. 1742–1749, 2018.
- [15] W. Liao, M. Hashimoto, S. Manabe, Y. Watanabe, S. Abe, K. Nakano, H. Sato, T. Kin, K. Hamada, M. Tampo, and Y. Miyake, “Measurement and Mechanism Investigation of Negative and Positive Muon-Induced Upsets in 65-nm Bulk SRAMs,” *IEEE Transactions on Nuclear Science*, vol. 65, no. 8, pp. 1734–1741, 2018.
- [16] S. Manabe, Y. Watanabe, W. Liao, M. Hashimoto, and S. Abe, “Estimation of Muon-Induced SEU Rates for 65-nm Bulk and UTBB-SOI SRAMs,” *IEEE Transactions on Nuclear Science*, vol. 66, no. 7, pp. 1398–1403, 2019.
- [17] W. Liao, M. Hashimoto, S. Manabe, S. Abe, and Y. Watanabe, “Similarity Analysis on Neutron- and Negative Muon-Induced MCUs in 65-nm Bulk SRAM,” *IEEE Transactions on Nuclear Science*, vol. 66, no. 7, pp. 1390–1397, 2019.
- [18] W. Liao, M. Hashimoto, S. Manabe, Y. Watanabe, S. Abe, K. Nakano, H. Takeshita, M. Tampo, S. Takeshita, and Y. Miyake, “Negative and Positive Muon-Induced SEU Cross Sections in 28-nm and 65-nm Planar Bulk CMOS SRAMs,” in *Proc. 2019 IEEE International Reliability Physics Symposium (IRPS)*, 2019, pp. 1–5.
- [19] S. E. Sobottka and E. L. Wills, “Energy Spectrum of Charged Particles Emitted Following Muon Capture in  $\text{Si}^{28}$ ,” *Physical Review Letters*, vol. 20, no. 12, pp. 596–598, 1968.
- [20] E. Fermi and E. Teller, “The Capture of Negative Mesotrons in Matter,” *Physical Review*, vol. 72, no. 5, pp. 399–408, 1947.
- [21] W. R. Leo, “Techniques for Nuclear and Particle Physics Experiments”. *Springer-Verlag*, 1987.
- [22] M. K. Kubo, “Non-destructive Elemental Analysis Using Negative Muon,” *Journal of the Physical Society of Japan*, vol. 85, no. 9, p. 091 015, 2016.

- [23] K. Terada, A. Sato, K. Ninomiya, Y. Kawashima, K. Shimomura, G. Yoshida, Y. Kawai, T. Osawa, and S. Tachibana, “Non-destructive elemental analysis of a carbonaceous chondrite with direct current Muon beam at MuSIC,” *Scientific Reports*, vol. 7, no. 15478, 2017.
- [24] Y. Miyake, K. Nishiyama, N. Kawamura, P. Strasser, S. Makimura, A. Koda, K. Shimomura, H. Fujimori, K. Nakahara, R. Kadono, M. Kato, S. Takeshita, W. Higemoto, K. Ishida, T. Matsuzaki, Y. Matsuda, and K. Nagamine, “J-PARC muon source, MUSE,” *Nuclear Instruments and Methods in Physics Research Section A: Accelerators, Spectrometers, Detectors and Associated Equipment*, vol. 600, no. 1, pp. 22–24, 2009.
- [25] Y. Miyake, K. Shimomura, N. Kawamura, P. Strasser, A. Koda, S. Makimura, H. Fujimori, Y. Ikedo, K. Nakahara, S. Takeshita, M. Kato, K. Kojima, Y. Kobayashi, K. Nishiyama, R. Kadono, W. Higemoto, T. U. Ito, K. Ninomiya, K. Kubo, and K. Nagamine, “J-PARC Muon Facility, MUSE,” *Physics Procedia*, vol. 30, pp. 46–49, 2012.
- [26] T. Sato, Y. Iwamoto, S. Hashimoto, T. Ogawa, T. Furuta, S. Abe, T. Kai, P.-E. Tsai, N. Matsuda, H. Iwase, N. Shigyo, L. Sihver, and K. Niita, “Features of Particle and Heavy Ion Transport code System (PHITS) version 3.02,” *Journal of Nuclear Science and Technology*, vol. 55, no. 6, pp. 684–690, 2018.
- [27] N. Seifert, S. Jahinuzzaman, J. Velamala, R. Ascazubi, N. Patel, B. Gill, J. Basile, and J. Hicks, “Soft Error Rate Improvements in 14-nm Technology Featuring Second-Generation 3D Tri-Gate Transistors,” *IEEE Transactions on Nuclear Science*, vol. 62, no. 6, pp. 2570–2577, 2015.
- [28] A. Sato, Y. Kuno, H. Sakamoto, Y. Hino, N. Tran, N. Minh Truong, S. Cook, R. D’Arcy, M. Fukuda, K. Hatanaka, Y. Mori, T. Ogitsu, A. Yamamoto, and M. Yoshida, “MuSIC, the world’s highest intense DC muon beam using a pion capture system,” in *Proc. 2nd International Particle Accelerator Conference (IPAC)*, 2011, pp. 820–822.
- [29] RCNP homepage. <http://www.rcnp.osaka-u.ac.jp/>.
- [30] Y. Matsumoto, M. Fukuda, K. Hatanaka, M. Ieiri, Y. Kawashima, Y. Kohno, Y. Kuno, M. Minakawa, S. Morinobu, Y. Nakazawa, H. Sakamoto, A. Sato, K. Takahisa, and H. Ueda, “A New DC Muon Beam Line at RCNP, Osaka University,” in *Proc. 6th International Particle Accelerator Conference (IPAC)*, 2015, pp. 2537–2540.
- [31] D. Tomono (private communication).
- [32] LUPO DAQ Master Module Rev. 1.1. [https://ribf.riken.jp/RIBFDAQ/index.php?plugin=attach&refer=DAQ\%2FDownload&openfile=lupo\\_daqmaster\\_rev1.1e.pdf](https://ribf.riken.jp/RIBFDAQ/index.php?plugin=attach&refer=DAQ\%2FDownload&openfile=lupo_daqmaster_rev1.1e.pdf).
- [33] Y. Tosaka, H. Kanata, S. Satoh, and T. Itakura, “Simple method for estimating neutron-induced soft error rates based on modified BGR model,” *IEEE Electron Device Letters*, vol. 20, no. 2, pp. 89–91, 1999.
- [34] A. Suzuki, “Relative Intensities of K and L Series of Muonic X Rays,” *Physical Review Letters*, vol. 19, no. 18, pp. 1005–1009, 1967.

# Acknowledgments

First and foremost, I would like to express my gratitude to my supervisor Professor Yukinobu Watanabe. Without his guidance and persistent help, this thesis would not have been possible. I have learned a lot from him not only concerning research but also logical thinking and philosophy. His comments and supports are always valuable and precious.

I wish to thank very much Associate professor Tadahiro Kin for his help on my study. I had several opportunities to work on the class together as a teaching assistant, however I'm sorry I could not help much.

I am deeply grateful to Professor Masanori Hashimoto and Dr. Wang Liao at the Department of Information System Engineering, Osaka University for providing the device board and their helpful comments about device physics. I owe a very important debt to Assistant Professor Megumi Niikura, Mr. Takeshi Saito at the Department of Physics, the University of Tokyo for their cooperation of construction of DAQ system and advice for my analysis of this work. I would like to offer my special thanks to Assistant Professor Akira Sato and Dr. Dai Tomono at the Research Center for Nuclear Physics and Assistant Professor Kazuhiko Ninomiya at the Graduate School of Science, Osaka University for their willingness for us to use their accelerator and detectors.

I wish to thank very much for Seiya Manabe, Junya Kuroda, Takuya Murota, Naoki Yamaguchi and Hiroya Fukuda at same research group. Seiya Manabe has been kindly and carefully taught me various things related to research since I was assigned to this laboratory. Junya Kuroda works hard together as the same period. I have interacted with Takuya Murota, Naoki Yamaguchi and Hiroya Fukuda as juniors in same group, however I also have learned a lot from them.

My great thanks are expressed to Ms. Rumiko Koga for her help in office work. I also would like to thank all other members in the Watanabe-Kin laboratory, Keita Nakano, Kawchar Patwary, Shunsuke Sato, Hikaru Sato, Katsumi Aoki, Hayato Takeshita, Satoko Kamei, Tomohiro Komori, Keiichiro Shiokawa, Kosuke Yoshinami, Miyuki Uematsu, Naoya Okamoto, Yuji Shinjo, Yu Horai, Tatsuhiko Miyatake, Mary Alfonse, Masaya Yamaguchi, Misaki Saitsu and Ryuhei Takahashi.

Finally, I would like to express my gratitude to my family. Without their supports, I could not complete this work.

This work was supported in part by JSPS KAKENHI under Grant JP16H03906 and in part by JST-OPERA Program, Japan, under Grant JPMJOP1721.